N to Δ electromagnetic transition form factors from lattice QCD

C. Alexandrou,[1] Ph. de Forcrand,[2] Th. Lippert,[3] H. Neff,[4] J.W. Negele,[5] K. Schilling,[3] W. Schroers,[5] and A. Tsapalis[1]

[1]*Department of Physics, University of Cyprus, CY-1678 Nicosia, Cyprus*
[2]*ETH-Zürich, CH-8093 Zürich, and CERN Theory Division, CH-1211 Geneva 23, Switzerland*
[3]*Department of Physics, University of Wuppertal, D-42097 Wuppertal, Germany*
[4]*Institute of Accelerating Systems and Applications, University of Athens, Athens, Greece*
and Physics Department, Boston University, Boston, Massachusetts 02215, USA
[5]*Center for Theoretical Physics, Laboratory for Nuclear Science and Department of Physics, Massachusetts Institute of Technology,*
Cambridge, Massachusetts 02139, USA

The magnetic dipole, the electric quadrupole, and the Coulomb quadrupole amplitudes for the transition $\gamma N \rightarrow \Delta$ are evaluated both in quenched lattice QCD at $\beta = 6.0$ and using two dynamical Wilson fermions simulated at $\beta = 5.6$. The dipole transition form factor is accurately determined at several values of momentum transfer. On the lattices studied in this work, the electric quadrupole amplitude is found to be nonzero, yielding a negative value for the ratio R_{EM} of electric quadrupole to magnetic dipole amplitudes at three values of momentum transfer.

I. INTRODUCTION

Recent photoproduction experiments on the nucleon at Bates [1] and Jefferson Lab [2] have produced accurate measurements on the ratios of electric and Coulomb quadrupole amplitudes to the magnetic dipole amplitude. Nonvanishing values for these ratios are thought to be connected with nucleon deformation.

Deformation is a common phenomenon in nuclear and atomic physics. Classically, the multiphoton coincidence experiment of taking a flash photograph or observing an illuminated object distinguishes a deformed dumbbell from a spherically symmetric sphere. Quantum mechanically, a multiphoton coincidence experiment could also determine that a $J=0$ ground state of a diatomic molecule has a deformed shape. However, usually in electromagnetic probes of microscopic systems, we are constrained to make measurements associated with one-photon exchange, corresponding to a matrix element of a one-body operator. In the case of a diatomic molecule, the one-body charge density of the $J=0$ state is spherically symmetric and cannot reveal the deformation that is present in the system.

In many cases, however, when a nuclear or atomic system is well approximated by a deformed intrinsic state, it is still possible to observe its deformation using a one-body electromagnetic operator. We consider here the lowest order electric multipole, the quadrupole moment. For an axially deformed object, the quadrupole moment in the body-fixed intrinsic frame is given by

$$Q_0 = \int d^3 r \rho(\mathbf{r})(3z^2 - r^2) \tag{1}$$

where $\rho(r)$ is the charge density distribution. If Q_0 is positive, the object is prolate with the polar axis longer than the equatorial axis. In contrast, for an oblate object with the polar axis shorter than the equatorial axis, the quadrupole moment is negative. For collective rotation of the deformed intrinsic state [3], the relation between the spectroscopic

quadrupole moment Q measured in the laboratory frame and the intrinsic quadrupole moment Q_0 in the body-fixed intrinsic frame is given by

$$Q = \frac{3K^2 - J(J+1)}{(J+1)(2J+3)} Q_0, \tag{2}$$

where J is the total angular momentum of the system in the lab, K is the projection of J onto the z axis of the body-fixed intrinsic frame, and we have considered the substate with azimuthal quantum number $M=J$. In the previous example of the $J=0$ diatomic molecule, although $Q_0 \neq 0$, Eq. (2) yields $Q=0$ so that the deformation, while present, is unobservable. Similarly, in the case of a nucleon with $J=1/2$, Q is zero although Q_0 may not be. However, for the Δ with $J=3/2$, Eq. (2) shows that a deformed intrinsic state can be detected by the spectroscopic quadrupole moment Q. The $E2$ and $C2$ transition moments between the $J=1/2$ nucleon and $J=3/2$ nucleon have the same property of revealing the presence of deformation in the nucleon, the Δ, or both, and in this work we calculate these moments in lattice QCD and provide direct evidence for this deformation.

The question whether the nucleon is deformed from a spherical shape was raised 20 years ago [4] and it is still unsettled. On the lattice, hadron wave functions obtained via density-density correlators can provide information about the deformation of particles of spin higher than 1/2 [5]. This approach yields no information about the deformation about the nucleon for the same reason as the vanishing of its spectroscopic quadrupole moment. This is why in lattice studies, as in experiment, one looks for quadrupole strength in the $\gamma N \rightarrow \Delta$ transition to extract information on the nucleon deformation.

State-of-the-art lattice QCD calculations can yield model-independent results for these matrix elements and provide direct comparison with experiment. Spin-parity selection rules allow a magnetic dipole $M1$, an electric quadrupole $E2$, and a Coulomb quadrupole $C2$ amplitude. If both the nucleon and the Δ are spherical, then $E2$ and $C2$ are ex-

pected to be zero. Although $M1$ is indeed the dominant amplitude, there is mounting experimental evidence over a range of momentum transfer that $E2$ and $C2$ are nonzero [1,2]. A recent analysis of experimental results on the values of $E2/M1$ and $C2/M1$ is shown to be incompatible with a spherical nucleon [7].

Understanding the origin of a nonzero deformation is an important theoretical issue, which depends on QCD dynamics. The physical origin of nonzero $E2$ and $C2$ amplitudes is attributed to different mechanisms in the various models: In the constituent nonrelativistic quark model the deformation was originally explained by the color-magnetic hyperfine interquark potential arising from one-gluon exchange and producing a D-state admixture in the singlet-quark wave functions of the nucleon and the Δ [4]. The deformation due to the hyperfine interaction was also studied in "relativized" quark models. In both cases the deformation obtained, measured by the ratio $E2/M1$, is smaller than that found experimentally.

In the context of the constituent quark model, it was recently proposed that elimination of gluonic and quark-antiquark pairs leads to two-body contributions in the charge and vector current operators that produce a nonzero quadrupole moment in agreement with experiment using only s-wave functions for the nucleon and the Δ [6]. In cloudy nonrelativistic models [6] as well as in chiral or cloudy bag models [8], the deformation arises because of the asymmetric pion cloud, whereas in soliton models it is thought to be due to the nonlinear pion field interactions. Most of the results obtained in cloudy baryon models predict values smaller than the experimentally measured ones suggesting that the deformation cannot be entirely attributed to the pion cloud. This is in agreement with lattice results [5] where a nonzero deformation is observed in the case of the rho meson even in the quenched approximation where pion cloud contributions are omitted.

In the present work we will compare quenched and unquenched results for the transition matrix element $\gamma N \rightarrow \Delta$ in order to examine sea quark contributions to the deformation [9]. An early, pioneering lattice QCD study [10] with a limited number of quenched configurations yielded an inconclusive result for the ratio of the electric quadrupole to magnetic dipole amplitudes, referred to as EMR or R_{EM}, since a zero value could not be statistically excluded. However, the theoretical framework that it provided is still applicable, and we will apply similar techniques to the present study making a number of improvements. (i) We use smearing techniques, which very effectively filter the ground state so that the time-independent physical observables can be extracted from the correlators. (ii) The quenched calculation is done on two volumes at the same parameters to check the volume dependence of the results. (iii) Using a large quenched lattice allows us to simulate smaller quark masses, the lightest giving a ratio of pion to rho mass of 50%. (iv) For each lattice momentum transfer **q** we calculate the multipoles in the rest frames both of the nucleon and of the Δ. These two different choices of kinematics enable the evaluation of the transition form factors at two different four-momentum transfers. (v) We study dynamical quark effects by evaluating the form
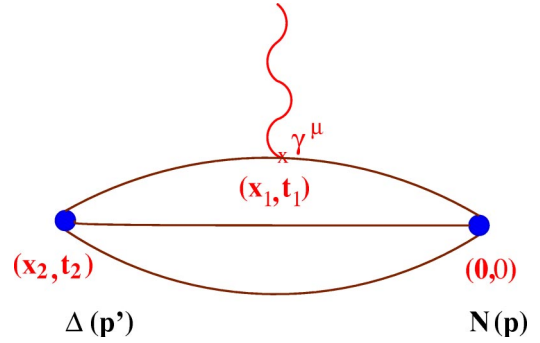

FIG. 1. $N\gamma \rightarrow \Delta$ matrix element. The photon couples to one of the quarks in the nucleon at a fixed time t_1 to produce a Δ.

factors using the SESAM configurations [11] that were produced at $\beta = 5.6$ on a lattice of size $16^3 \times 32$ using hybrid Monte Carlo simulations for two degenerate flavors of dynamical Wilson fermions. (vi) In all cases we use more configurations to improve the statistics.

II. LATTICE MATRIX ELEMENTS

The current matrix element for the $\gamma N \rightarrow \Delta$ transition with on-shell nucleon and Δ states and real or virtual photons is shown schematically in Fig. 1. It has the form [12]

$$\langle \Delta(p',s') | j_\mu | N(p,s) \rangle = i \sqrt{\frac{2}{3}} \left(\frac{m_\Delta m_N}{E_\Delta(\mathbf{p}') E_N(\mathbf{p})} \right)^{1/2}$$
$$\times \bar{u}_\tau(p',s') \mathcal{O}^{\tau\mu} u(p,s) \quad (3)$$

where $p(s)$ and $p'(s')$ denote initial and final momenta (spins) and $u_\tau(p',s')$ is a spin vector in the Rarita-Schwinger formalism.

The operator $\mathcal{O}^{\tau\mu}$ can be decomposed in terms of the Sachs form factors as

$$\mathcal{O}^{\tau\mu} = \mathcal{G}_{M1}(q^2) K_{M1}^{\tau\mu} + \mathcal{G}_{E2}(q^2) K_{E2}^{\tau\mu} + \mathcal{G}_{C2}(q^2) K_{C2}^{\tau\mu}, \quad (4)$$

where the magnetic dipole $\mathcal{G}_{M1}$, the electric quadrupole $\mathcal{G}_{E2}$, and the Coulomb quadrupole $\mathcal{G}_{C2}$, form factors depend on the momentum transfer $q^2 = (p' - p)^2$. The kinematical functions $K^{\tau\mu}$ depend on p, p', M_N, and M_Δ and their expressions are given in Ref. [12]. The reason for using this parametrization for a lattice computation, as pointed out in Ref. [10], is that the Sachs form factors do not depend strongly on the difference between the nucleon and the Δ mass. From the Sachs form factors one can evaluate the ratio $E2/M1$ referred to above as EMR or R_{EM}, and the analogous ratio of the Coulomb quadrupole amplitude to the magnetic dipole amplitude $C2/M1$, known as CMR or R_{SM}, which are the target of recent experiments. Using the relations given in Refs. [12,13] the ratios R_{EM} and R_{SM} in the rest frame of the Δ are obtained from the Sachs form factors via

$$R_{EM} = -\frac{\mathcal{G}_{E2}(q^2)}{\mathcal{G}_{M1}(q^2)} \quad (5)$$

and

$$R_{SM} = -\frac{|\mathbf{q}|}{2m_\Delta}\frac{\mathcal{G}_{C2}(q^2)}{\mathcal{G}_{M1}(q^2)}. \qquad (6)$$

The lattice construction of the appropriate matrix elements for the evaluation of these form factors follows closely that of Ref. [10]. The computationally most demanding part in this evaluation is the calculation of the three-point correlation function that corresponds to the diagram shown in Fig. 1 and it is given by

$$\langle G_\sigma^{\Delta j^\mu N}(t_2,t_1;\mathbf{p}',\mathbf{p};\Gamma)\rangle$$

$$= \sum_{\mathbf{x}_2,\,\mathbf{x}_1} \exp(-i\mathbf{p}'\cdot\mathbf{x}_2)\exp[+i(\mathbf{p}'-\mathbf{p})\cdot\mathbf{x}_1]\Gamma^{\beta\alpha}$$

$$\times\langle\Omega|T[\chi_\sigma^\alpha(\mathbf{x}_2,t_2)j^\mu(\mathbf{x}_1,t_1)\bar\chi^\beta(\mathbf{0},0)]|\Omega\rangle, \qquad (7)$$

where an initial state with the quantum numbers of the nucleon is created at time zero and the final state with the quantum numbers of the Δ is annihilated at a later time t_2. The photon couples to one of the quarks in the nucleon at an intermediate time t_1 producing a Δ. The corresponding three-point correlation function for the transition $\Delta\to\gamma N$ is given by

$$\langle G_\sigma^{Nj^\mu\Delta}(t_2,t_1;\mathbf{p}',\mathbf{p};\Gamma)\rangle$$

$$= \sum_{\mathbf{x}_2,\,\mathbf{x}_1} \exp(-i\mathbf{p}'\cdot\mathbf{x}_2)\exp[+i(\mathbf{p}'-\mathbf{p})\cdot\mathbf{x}_1]$$

$$\times\Gamma^{\beta\alpha}\langle\Omega|T[\chi^\alpha(\mathbf{x}_2,t_2)j^\mu(\mathbf{x}_1,t_1)\bar\chi_\sigma^\beta(\mathbf{0},0)]|\Omega\rangle. \qquad (8)$$

For the spin-$\frac{1}{2}$ source, $\chi^p(\mathbf{x},t)$, and the spin-$\frac{3}{2}$ source, $\chi_\sigma^{\Delta^+}(\mathbf{x},t)$, we use the interpolating fields

$$\chi^p(x) = \epsilon^{abc}[u^{Ta}(x)C\gamma_5 d^b(x)]u^c(x), \qquad (9)$$

$$\chi_\sigma^{\Delta^+}(x) = \frac{1}{\sqrt{3}}\epsilon^{abc}\{2[u^{Ta}(x)C\gamma_\sigma d^b(x)]u^c(x)$$

$$+[u^{Ta}(x)C\gamma_\sigma u^b(x)]d^c(x)\}, \qquad (10)$$

and for the projection matrices for the Dirac indices

$$\Gamma_i = \frac{1}{2}\begin{pmatrix}\sigma_i & 0\\ 0 & 0\end{pmatrix}, \quad \Gamma_4 = \frac{1}{2}\begin{pmatrix}I & 0\\ 0 & 0\end{pmatrix}. \qquad (11)$$

For large Euclidean time separations $t_2-t_1\gg 1$ and $t_1\gg 1$, the time dependence and field normalization constants are canceled in the following ratio [10]:

$$R_\sigma(t_2,t_1;\mathbf{p}',\mathbf{p};\Gamma;\mu) = \left[\frac{\langle G_\sigma^{\Delta j^\mu N}(t_2,t_1;\mathbf{p}',\mathbf{p};\Gamma)\rangle\langle G_\sigma^{Nj^\mu\Delta}(t_2,t_1;-\mathbf{p},-\mathbf{p}';\Gamma^\dagger)\rangle}{\langle\delta_{ij}G_{ij}^{\Delta\Delta}(t_2,\mathbf{p}';\Gamma_4)\rangle\langle G^{NN}(t_2,-\mathbf{p};\Gamma_4)\rangle}\right]^{1/2} \stackrel{t_2-t_1\gg 1,t_1\gg 1}{\Rightarrow} \Pi_\sigma(\mathbf{p}',\mathbf{p};\Gamma;\mu), \qquad (12)$$

where G^{NN} and $G_{ij}^{\Delta\Delta}$ are the nucleon and Δ two-point functions given, respectively, by

$$\langle G^{NN}(t,\mathbf{p};\Gamma)\rangle = \sum_{\mathbf{x}} e^{-i\mathbf{p}\cdot\mathbf{x}}\Gamma^{\beta\alpha}\langle\Omega|T\chi^\alpha(\mathbf{x},t)\bar\chi^\beta(\mathbf{0},0)|\Omega\rangle,$$

$$\langle G_{\sigma\tau}^{\Delta\Delta}(t,\mathbf{p};\Gamma)\rangle = \sum_{\mathbf{x}} e^{-i\mathbf{p}\cdot\mathbf{x}}\Gamma^{\beta\alpha}\langle\Omega|T\chi_\sigma^\alpha(\mathbf{x},t)\bar\chi_\tau^\beta(\mathbf{0},0)|\Omega\rangle. \qquad (13)$$

The phase in Eq. (12) is the same as that of $G_\sigma^{\Delta j^\mu N}(t_2,t_1;\mathbf{p}',\mathbf{p})$ since formally we have

$$\Pi_\sigma(\mathbf{p}',\mathbf{p};\Gamma;\mu) = \left(\frac{E_\Delta+m_\Delta}{E_\Delta}\right)^{-1/2}\left(1+\frac{\mathbf{q}^2}{3m_\Delta^2}\right)^{-1/2}$$

$$\times\left(\frac{E_N+m_N}{2E_N}\right)^{-1/2}\frac{\langle G_\sigma^{\Delta j^\mu N}(t_2,t_1;\mathbf{p}',\mathbf{p};\Gamma)\rangle}{Z_N Z_\Delta e^{-E_\Delta(t_2-t_1)}e^{-E_N t_1}}. \qquad (14)$$

We use the lattice conserved electromagnetic current $j^\mu(x)$ given by

$$j^\mu(x) = \sum_f Q_f\kappa_f\{\bar\psi^f(x+\hat\mu)(1+\gamma_\mu)U^{\mu\dagger}(x)\psi^f(x)$$

$$-\bar\psi^f(x)(1-\gamma_\mu)U^\mu(x)\psi^f(x+\hat\mu)\}, \qquad (15)$$

symmetrized on site x by taking $j^\mu(x)\to[j^\mu(x)+j^\mu(x-\hat\mu)]/2$, where Q_f is the charge of a quark of flavor f and κ_f is its hopping parameter.

In the nucleon laboratory frame $\mathbf{p}=0$ and $\mathbf{p}'=\mathbf{q}$. The Sachs form factors can be extracted from the plateau values of $\Pi_\sigma(\mathbf{p}',\mathbf{p};\Gamma;\mu)$ for specific combinations of the matrices Γ and the Δ vector indices σ. The expressions for general momentum transfer $\mathbf{q}$ are obtained using the standard Euclidean nonrelativistic representation for the γ matrices [14] with $\epsilon^{1234}=1$. The kinematical functions $K^{\tau\mu}$ in Euclidean space are given by

$$K_{M1}^{\tau\mu} = -\frac{3}{(m_\Delta+m_N)^2+Q^2}\frac{(m_\Delta+m_N)}{2m_N}i\epsilon^{\tau\mu\alpha\beta}p^\alpha p'^\beta,$$

$$K_{E2}^{\tau\mu} = -K_{M1}^{\tau\mu}+6\Omega^{-1}(Q^2)\frac{(m_\Delta+m_N)}{2m_N}$$

$$\times 2i\gamma_5\epsilon^{\tau\lambda\alpha\beta}p^\alpha p'^\beta\epsilon^{\mu\lambda\gamma\delta}p^\gamma p'^\delta,$$

$$K_{C2}^{\tau\mu} = -6\Omega^{-1}(Q^2)\frac{(m_\Delta+m_N)}{2m_N}i\gamma_5 Q^\tau(Q^2 P^\mu - Q\cdot P Q^\mu),$$

(16)

with $\Omega(Q^2)=[(m_\Delta+m_N)^2+Q^2][(m_\Delta-m_N)^2+Q^2]$ and $\mathbf{Q}=\mathbf{q}$, where $Q^4=iq^0$ is the lattice momentum transfer giving $Q^2=-q^2$. By p^α and p'^β we now denote Euclidean space momenta defined analogously to Q^μ. The Rarita-Schwinger spin sum for the Δ in Euclidean space is given by

$$\sum_s u_\sigma(p,s)\bar{u}_\tau(p,s)=\frac{-i\gamma\cdot p+m_\Delta}{2m_\Delta}\left[\delta_{\sigma\tau}+\frac{2p_\sigma p_\tau}{3m_\Delta^2}\right.$$
$$\left. -i\frac{p_\sigma\gamma_\tau-p_\tau\gamma_\sigma}{3m_\Delta}-\frac{1}{3}\gamma_\sigma\gamma_\tau\right]$$

(17)

and the Dirac spin sum

$$\sum_s u(p,s)\bar{u}(p,s)=\frac{-i\gamma\cdot p+m_N}{2m_N}.$$

(18)

We generalize in what follows the expressions of Ref. [10] to allow momentum transfers in any spatial direction. By selecting the time component of the current the $\mathcal{G}_{C2}$ form factor is extracted from

$$\mathcal{G}_{C2}=C(\mathbf{q}^2)\left[\frac{2m_\Delta}{\delta^{lk}\mathbf{q}^2-q^k q^l(1+2E_\Delta/m_\Delta)}\right]\Pi_l(\mathbf{q},0;i\Gamma_k;4),$$

$$C(\mathbf{q}^2)=\sqrt{\frac{3}{2}}\frac{4E_\Delta m_N}{m_N+m_\Delta}\left(\frac{E_\Delta+m_\Delta}{E_\Delta}\right)^{1/2}\left(1+\frac{\mathbf{q}^2}{3m_\Delta^2}\right)^{1/2},$$

(19)

where $E_\Delta=\sqrt{\mathbf{p'}^2+m_\Delta^2}$ and the indices k and l denote spatial directions. By selecting the spatial component of the current the $\mathcal{G}_{M1}$ and $\mathcal{G}_{E2}$ form factors are extracted from

$$\mathcal{G}_{M1}=C(\mathbf{q}^2)\epsilon^{\sigma lk4}\frac{1}{q^k}\Pi_\sigma(\mathbf{q},0;i\Gamma_4;l)$$

$$=C(\mathbf{q}^2)\frac{1}{(q^k)^2-(q^l)^2}\left(q^k\Pi_l(\mathbf{q},0;\Gamma_k;l)\right.$$

$$-q^l\Pi_k(\mathbf{q},0;\Gamma_l;k)-\frac{m_\Delta}{E_\Delta}[q^k\Pi_k(\mathbf{q},0;\Gamma_l;l)$$

$$\left. -q^l\Pi_l(\mathbf{q},0;\Gamma_k;k)]\right)$$

(20)

and

$$\mathcal{G}_{E2}=\frac{C(\mathbf{q}^2)}{3}\frac{1}{(q^k)^2-(q^l)^2}$$

$$\times\left(q^k\Pi_l(\mathbf{q},0;\Gamma_k;l)-q^l\Pi_k(\mathbf{q},0;\Gamma_l;k)\right.$$

$$\left. +\frac{m_\Delta}{E_\Delta}[q^k\Pi_k(\mathbf{q},0;\Gamma_l;l)-q^l\Pi_l(\mathbf{q},0;\Gamma_k;k)]\right)$$

(21)

provided $q^k\neq q^l$. If we consider a momentum transfer that has zero component along the current direction, Eqs. (20) and (21) simplify to

$$\binom{\mathcal{G}_{M1}}{3\mathcal{G}_{E2}}=\frac{C(\mathbf{q}^2)}{q^k}\left(\Pi_l(\mathbf{q},0;\Gamma_k;l)\mp\frac{m_\Delta}{E_\Delta}\Pi_k(\mathbf{q},0;\Gamma_l;l)\right).$$

(22)

Another possibility is to extract the transition form factors by using, instead of R_σ, the ratio

$$R_\sigma^{(1)}(t_2,t_1;\mathbf{p'},\mathbf{p};\Gamma;\mu)=\frac{\langle G_\sigma^{\Delta j^\mu N}(t_2,t_1;\mathbf{p'},\mathbf{p};\Gamma)\rangle}{\langle\delta_{ij}G_{ij}^{\Delta\Delta}(t_2,\mathbf{p'};\Gamma_4)\rangle[\langle G^{NN}(2t_1,\mathbf{p};\Gamma_4)\rangle/\langle\delta_{ij}G_{ij}^{\Delta\Delta}(2t_1,\mathbf{p'};\Gamma_4)\rangle]^{1/2}},$$

(23)

or equivalently

$$R_\sigma^{(2)}(t_2,t_1;\mathbf{p'},\mathbf{p};\Gamma;\mu)=\frac{\langle G_\sigma^{Nj^\mu\Delta}(t_2,t_1;\mathbf{p'},\mathbf{p};\Gamma)\rangle}{\langle G^{NN}(t_2,\mathbf{p'};\Gamma_4)\rangle[\langle\delta_{ij}G_{ij}^{\Delta\Delta}(2t_1,\mathbf{p};\Gamma_4)\rangle/\langle G^{NN}(2t_1,\mathbf{p'};\Gamma_4)\rangle]^{1/2}}.$$

(24)

In this work we choose the current along the z direction and consider momentum transfers along the x axis. In particular we consider the lowest allowed lattice momentum transfer $\mathbf{q}=(2\pi/Na,0,0)$, where a is the lattice spacing and N the spatial lattice size, with the exception of the large quenched lattice, where we also consider momentum transfer $\mathbf{q}=(4\pi/Na,0,0)$. For our choice of the momentum $\mathbf{q}$ it is reasonable to take in Eqs. (12), (23), and (24) the more symmetric combination $3/2(G_{22}^{\Delta\Delta}+G_{33}^{\Delta\Delta})$ instead of $\delta_{ij}G_{ij}^{\Delta\Delta}$. With this replacement the second square root involving $\mathbf{q}^2$ in the overall factor $C(\mathbf{q}^2)$ given in Eq. (19) is absent. Using the fact that the momentum transfer has a component only in the x direction Eqs. (19) and (22) simplify to

$$\mathcal{G}_{C2}^{(a)}=C_0\frac{m_\Delta}{\mathbf{q}^2}\frac{m_\Delta}{E_\Delta}\Pi_1(\mathbf{q},0;-i\Gamma_1;4),\tag{25}$$

$$\mathcal{G}_{C2}^{(b)}=C_0\frac{2m_\Delta}{\mathbf{q}^2}\Pi_2(\mathbf{q},0;i\Gamma_2;4)$$

$$=C_0\frac{2m_\Delta}{\mathbf{q}^2}\Pi_3(\mathbf{q},0;i\Gamma_3;4),\tag{26}$$

and

$$\mathcal{G}_{M1}^{(a)}=C_0\frac{1}{|\mathbf{q}|}\Pi_2(\mathbf{q},0;i\Gamma_4;3),\tag{27}$$

$$\mathcal{G}_{M1}^{(b)}=C_0\frac{1}{|\mathbf{q}|}\left(\Pi_3(\mathbf{q},0;\Gamma_1;3)-\frac{m_\Delta}{E_\Delta}\Pi_1(\mathbf{q},0;\Gamma_3;3)\right),\tag{28}$$

$$\mathcal{G}_{E2}^{(a)}=\frac{C_0}{3}\frac{1}{|\mathbf{q}|}(2\Pi_3(\mathbf{q},0;\Gamma_1;3)-\Pi_2(\mathbf{q},0;i\Gamma_4;3)),\tag{29}$$

$$\mathcal{G}_{E2}^{(b)}=\frac{C_0}{3}\frac{1}{|\mathbf{q}|}\left(\Pi_3(\mathbf{q},0;\Gamma_1;3)+\frac{m_\Delta}{E_\Delta}\Pi_1(\mathbf{q},0;\Gamma_3;3)\right),\tag{30}$$

where C_0 is obtained from $C(\mathbf{q}^2)$ given in Eq. (19) by omitting the second square root [15]. When the Δ is produced at rest, the factors m_Δ/E_Δ in Eqs. (25), (28), and (30) are absent and

$$C_0\rightarrow\sqrt{\frac{3}{2}\frac{4m_NE_N}{m_\Delta+m_N}}\sqrt{\frac{E_N+m_N}{E_N}}.$$

The resulting formulas then agree with those given in Ref. [10].

Smearing is essential for achieving ground state dominance before the signal from the time correlators is lost in the noisy large time limit. We use the gauge invariant Wuppertal smearing $d(x,t)\rightarrow d^{\text{smear}}(x,t)$ at the source and the sink. We smear the fermion interpolating fields according to [16,17]

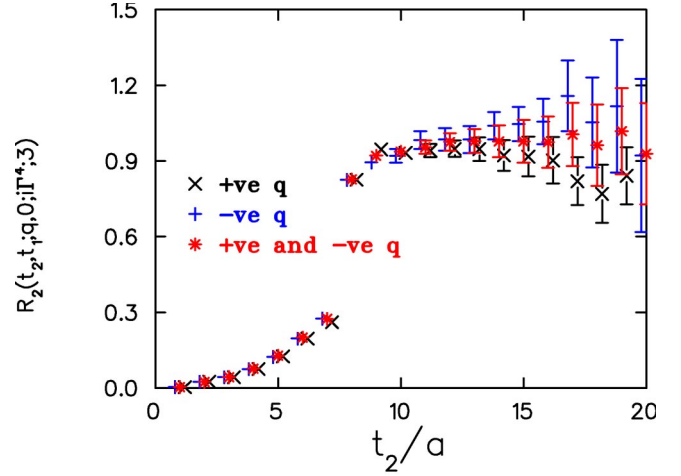$$d^{\text{smear}}(\mathbf{x},t)=\sum_\mathbf{z}F(\mathbf{x},\mathbf{z};U(t))d(\mathbf{z},t)\tag{31}$$

FIG. 2. The ratio $R_2(t_2,t_1;\mathbf{q},0;i\Gamma_4;3)$. Data with a photon carrying momentum $\mathbf{q}$ *and* $-\mathbf{q}$ averaged over 50 quenched configurations are denoted by the stars. Data with a photon carrying either positive or negative $\mathbf{q}$ averaged over 100 configurations are shown by the $\times$ and $+$ symbols, respectively. These results are for a lattice of size $32^3\times64$ at $\kappa=0.1558$. The current couples to the quark at $t_1/a=8$.

with the gauge invariant smearing function constructed from the hopping matrix H:

$$F(\mathbf{x},\mathbf{z};U(t))=(1+\alpha H)^n[\mathbf{x},\mathbf{z};U(t)],\tag{32}$$

where $H(\mathbf{x},\mathbf{z};U(t))=\Sigma_{i=1}^3[U_i(\mathbf{x},t)\delta_{\mathbf{x},\mathbf{y}-i}+U_i^\dagger(\mathbf{x}-i,t)\delta_{\mathbf{x},\mathbf{y}+i}]$. The parameters $\alpha=4.0$ and $n=50$ are tuned so as to optimize the overlap with the baryon states. Quark propagators with a photon insertion are computed with the sequential source technique. Therefore for the three-point functions we require two inversions with the second inversion having a momentum-dependent source. The sequential source technique requires that the photon couples to the quark at fixed time t_1 which is chosen large enough so that the nucleon and Δ ground states are identified. For the lattices used here we know from the nucleon and Δ two-point functions that for $t_1\geq5a$ the excited state contributions become negligible. We also make use of the equal weighting of the $\{U\}$ and $\{U^*\}$ gauge configurations in the lattice action [18] and the parity symmetry of our correlators to improve the plateau behavior of the reduced ratio $\Pi_\sigma(\mathbf{p}',\mathbf{p};\Gamma;\mu)$. For implementation of this procedure we need an additional sequential propagator with the photon carrying momentum $-\mathbf{q}$. To see the improvement, we compare in Fig. 2 the results obtained when for each configuration we consider the photon carrying either momentum $\mathbf{q}$ or $-\mathbf{q}$ to those obtained for the photon with momenta $\mathbf{q}$ *and* $-\mathbf{q}$ for equal statistics. As can be seen, for large time separations, the quality of the plateau obtained for the reduced ratio $\Pi_\sigma(\mathbf{p}',\mathbf{p};\Gamma;\mu)$ is improved when the equal reweighting of $\{U\}$ and $\{U^*\}$ is implemented, enabling us to fit over a larger range, far from the time insertion of the current. In all the results presented here this benefit is utilized: thus for each configuration the sequential propagator is inverted twice, once with the photon carrying momentum $\mathbf{q}$ and once carrying momentum $-\mathbf{q}$.
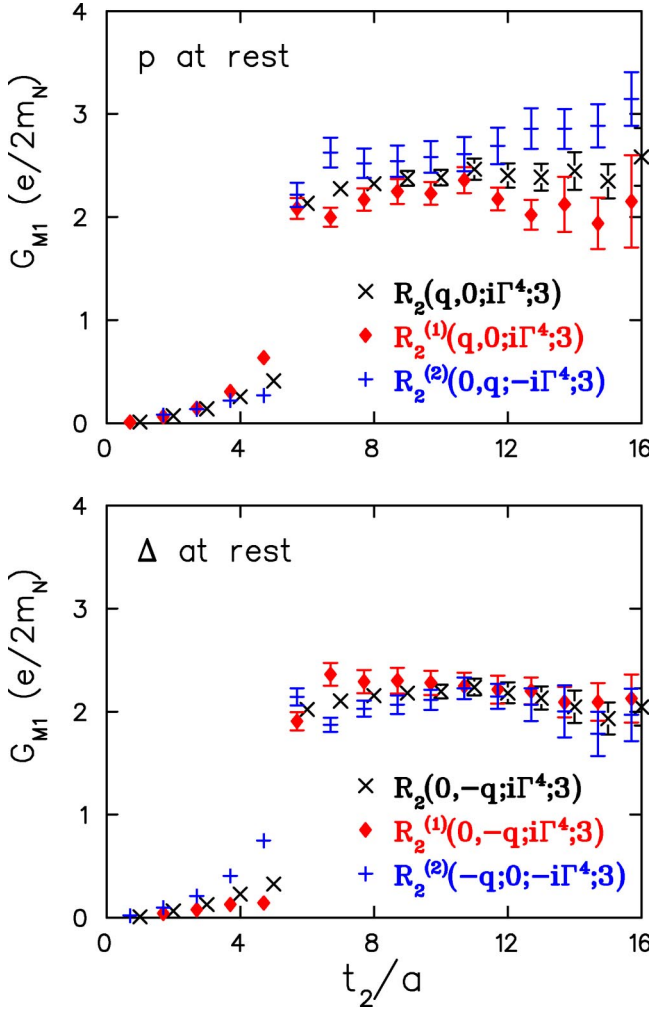
FIG. 3. $\mathcal{G}_{M1}^{(a)}$ in units of natural magnetons using the ratios R_σ ($\times$), $R_\sigma^{(1)}$ ($\blacklozenge$), and $R_\sigma^{(2)}$ ($+$) with the nucleon at rest (top) and with the Δ at rest (bottom) for dynamical quarks at $\kappa = 0.1565$. The current couples to the quark at $t_1/a = 6$.

FIG. 4. $\mathcal{G}_{E2}^{(a)}$ in units of natural magnetons extracted from Eq. (29) using the ratios R_σ ($\times$), $R_\sigma^{(1)}$ ($\blacklozenge$), and $R_\sigma^{(2)}$ ($+$) with the nucleon at rest (top) and with Δ at rest (bottom) for dynamical quarks at $\kappa = 0.1565$. The current couples to the quark at $t_1/a = 6$.

Unambiguous identification of the plateau region at large time separations from the source outweighs the additional costs.

The ratios given in Eqs. (12), (23), and (24) provide three ways for extracting the form factors. In Fig. 3 we compare these three possibilities for evaluating $\mathcal{G}_{M1}^{(a)}$. The plot illustrates the results for the unquenched case at $\kappa = 0.1565$—a similar behavior is observed in all cases. We consider two kinematically different cases: one where the nucleon has zero momentum and therefore the Δ carries momentum $\mathbf{q}$, and the other where the Δ is produced at rest and therefore the nucleon has momentum $-\mathbf{q}$. What is clearly seen for both kinematics is that R_σ as given in Eq. (12) yields the best plateau, which starts as early as two time slices away from the time where the current couples to the quark. In contrast, the other two definitions require five time slices to show convergence to the same value. Evidently excited state contributions come with the opposite sign in the matrix elements $\gamma N \to \Delta$ and $\Delta \to \gamma N$ canceling to a large extent in the ratio R_σ. The same conclusion is reached for $\mathcal{G}_{M1}^{(b)}$ extracted from
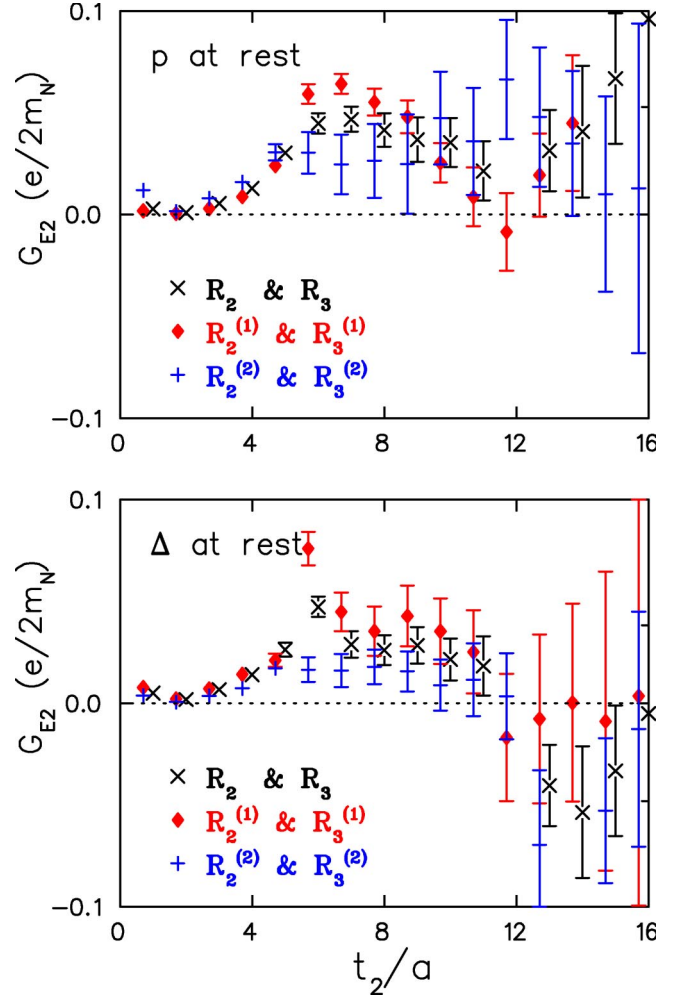
Eq. (28) (without the m_Δ/E_Δ factor when Δ is at rest). In Fig. 4 we show the analogous results for $\mathcal{G}_{E2}^{(a)}$ extracted from Eq. (29). Again the ratio R_σ yields an earlier plateau, which in this case is indispensable since the signal becomes too noisy beyond time separations $t_1 - t_2 \gtrsim 6/a$. Equation (30) provides an alternative way to extract the electric quadrupole form factor. However, the plateaus for the reduced ratios involved in the extraction of $\mathcal{G}_{E2}^{(b)}$ deteriorate when the nucleon is at rest leading to unreliable results. When the Δ is at rest, Eq. (30) produces a good plateau for the ratio R_σ, yielding results for $\mathcal{G}_{E2}^{(b)}$ consistent with those for $\mathcal{G}_{E2}^{(a)}$. Therefore in what follows Eq. (30) will be used only when the Δ is produced at rest to check consistency with the values obtained from Eq. (29). The ratio R_{EM} is evaluated using $\mathcal{G}_{E2}^{(a)}$ and $\mathcal{G}_{M1}^{(a)}$ since this is applicable for both types of kinematics. The systematic errors and noise become worse for $\mathcal{G}_{C2}$. When the Δ is produced in motion the ratio R_σ cannot be used since the correlators $G_\sigma^{\Delta j N}$ and $G_\sigma^{Nj\Delta}$ do not agree even in sign for time separations $t_2 - t_1 \lesssim 11/a$, and after that they are too noisy to be usable. This is seen in Fig. 5 where
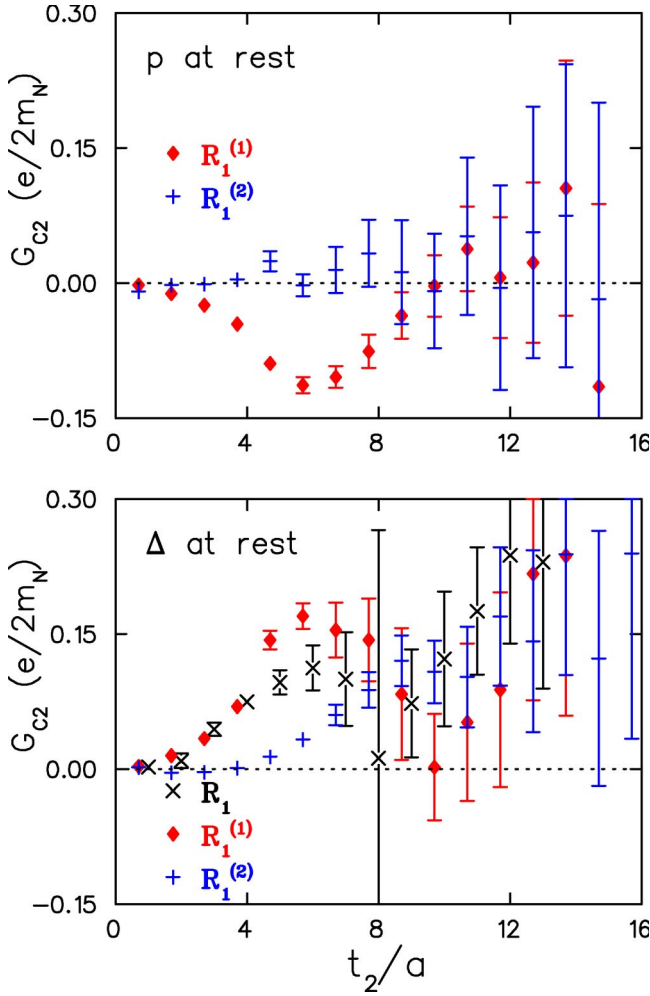
FIG. 5. $\mathcal{G}_{C2}^{(a)}$ in units of natural magnetons extracted from Eq. (25) using the ratios R_σ ($\times$), $R_\sigma^{(1)}$ ($\blacklozenge$), and $R_\sigma^{(2)}$ (+) with the nucleon at rest (top) and with Δ at rest (bottom) for dynamical quarks at $\kappa=0.1565$. The current couples to the quark at $t_1/a=6$.

we show results for $\mathcal{G}_{C2}^{(a)}$. The other two combinations that yield $\mathcal{G}_{C2}^{(b)}$ show at best equally poor results. When the Δ is produced at rest the signs are consistent and the ratio R_σ, although noisy, can be used to look for a plateau. In what follows we will attempt to fit over the plateau range only for the case when the Δ is at rest in order to provide an estimate on $\mathcal{G}_{C2}$ wherever possible.

In the case of the dominant amplitude $M1$ the definitions $\mathcal{G}_{M1}^{(a)}$ and $\mathcal{G}_{M1}^{(b)}$ can be used for both our kinematics and the results for $\mathcal{G}_{M1}^{(a)}$ and $\mathcal{G}_{M1}^{(b)}$ are directly compared in Fig. 6 for the SESAM lattice at $\kappa=0.1565$ at momentum transfer $\mathbf{q}=(2\pi/16a,0,0)$ both when the Δ is produced at rest and when the nucleon is at rest. In the Δ rest frame $\mathcal{G}_{M1}^{(a)}$ and $\mathcal{G}_{M1}^{(b)}$ are in perfect agreement with a plateau region that sets in as early as two time slices from the insertion of the current. When the Δ carries momentum, $\mathcal{G}_{M1}^{(a)}$ and $\mathcal{G}_{M1}^{(b)}$ agree for time separations $t_2-t_1\gtrsim4/a$, suggesting that contamination due to excited states is more severe when the Δ is produced in motion.
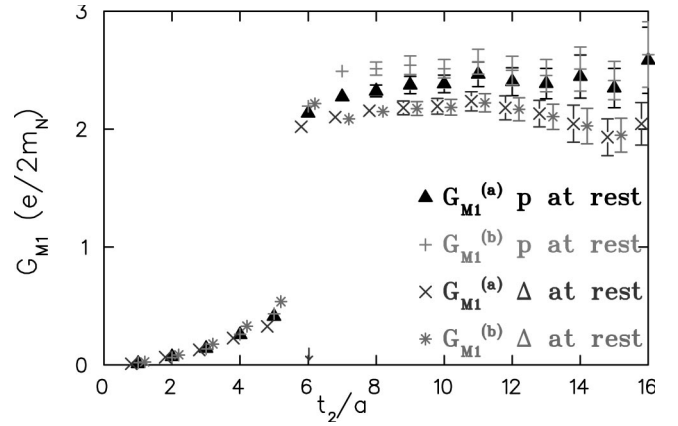

FIG. 6. $\mathcal{G}_{M1}$ in units of natural magnetons ($e/2m_N$) for the unquenched theory on a lattice of size $16^3\times32$ at $\kappa=0.1565$ and momentum transfer $\mathbf{q}=(2\pi/16a,0,0)$. Filled triangles and crosses denote results for $\mathcal{G}_{M1}^{(a)}$ [Eq. (27)] and $\mathcal{G}_{M1}^{(b)}$ [Eq. (28)], respectively, when the nucleon is at rest. The $\times$'s and stars denote, respectively, results for $\mathcal{G}_{M1}^{(a)}$ and $\mathcal{G}_{M1}^{(b)}$ when the Δ is produced at rest. They are shifted to the left and right of the results obtained when the nucleon is at rest for clarity. The photon is injected at $t_1/a=6$ as shown by the arrow.

Figures 7 and 8 show the corresponding results for $\mathcal{G}_{E2}$ and $\mathcal{G}_{C2}$. For both form factors the data become very noisy for time separations $t_2-t_1\gtrsim7/a$. However, for the case of the electric quadrupole we have a plateau region extending over four time slices, enabling us to extract a value for $\mathcal{G}_{E2}^{(a)}$ both for Δ static and for Δ carrying a momentum. When the Δ is produced at rest the reduced ratio needed for the extraction of $\mathcal{G}_{E2}^{(b)}$ shows similar plateau behavior as that obtained for $\mathcal{G}_{E2}^{(a)}$ whereas, as we already mentioned, when the Δ is not at rest this correlator is too noisy to be useful especially for the small quenched and unquenched lattices. The identification of the plateau region becomes particularly difficult for $\mathcal{G}_{C2}$. In Fig. 8 we show results for the ratio R_σ only for the case when the Δ is produced at rest since, as we have

FIG. 7. $\mathcal{G}_{E2}$ in natural magnetons for the unquenched theory on a lattice of size $16^3\times32$ at $\kappa=0.1565$ and momentum transfer $\mathbf{q}=(2\pi/16a,0,0)$. Filled triangles denote the results for $\mathcal{G}_{E2}^{(a)}$ when the nucleon is at rest. The $\times$'s and stars denote, respectively, results for $\mathcal{G}_{E2}^{(a)}$ and $\mathcal{G}_{E2}^{(b)}$ when the Δ is produced at rest. The rest of the notation is the same as that of Fig. 6.
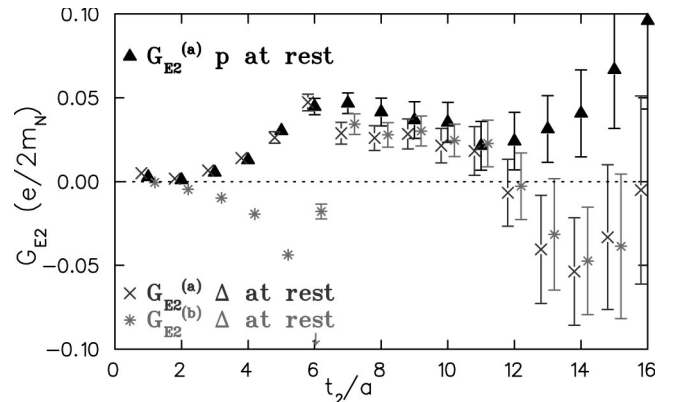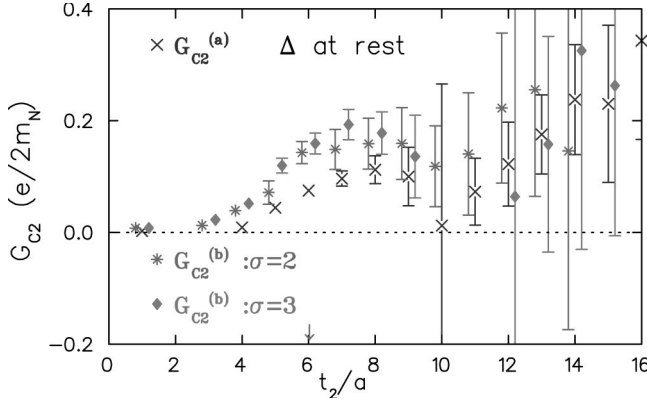
FIG. 8. $\mathcal{G}_{C2}$ in natural magnetons for the unquenched theory on a lattice of size $16^3 \times 32$ at $\kappa = 0.1565$ and momentum transfer **q** $= (2\pi/16a, 0, 0)$. We show only results for the Δ at rest. The ×'s denote the results for $\mathcal{G}_{C2}^{(a)}$ [without the factor m_Δ/E_Δ in Eq. (25)]; stars and diamonds denote results for $\mathcal{G}_{C2}^{(b)}$ using Eq. (26) with the Δ vector index $\sigma = 2$ and $\sigma = 3$, respectively. The rest of the notation is the same as that of Fig. 6.

already discussed, when the Δ has nonzero momentum the three-point functions fluctuate in sign, making the ratio R_σ unusable. From Fig. 8 it can be seen that the results obtained for $\mathcal{G}_{C2}^{(a)}$, involving matrix elements with the Δ vector index σ in the same direction as that of the momentum transfer, have overall smaller statistical errors as compared to those for $\mathcal{G}_{C2}^{(b)}$. In fact, for most cases, the ratio R_σ from Eq. (26)

can be determined only for small time separations $t_2 - t_1$, insufficient to neglect contributions from excited states. Therefore in what follows we will mostly use Eq. (25) to estimate $\mathcal{G}_{C2}$.

The behavior of the transition form factors shown in Figs. 6, 7, and 8 for the SESAM lattice at $\kappa = 0.1565$ is typical and it is observed for the other lattices and κ values.

III. RESULTS

The quenched calculation of the transition form factors is carried out at $\beta = 6.0$ using lattices of size $16^3 \times 32$ and $32^3 \times 64$. For the unquenched calculation we use the SESAM configurations at $\beta = 5.6$ on a lattice of size $16^3 \times 32$. We use Wilson fermions with hopping parameters κ given in Table I where we also list the values of the ratio of the pion mass to the rho mass. For all configurations, the number of which is given in Table I, we double the statistics in performing the calculation both for **q** and for $-$**q**.

To set the lattice spacing a in the quenched theory one can use the well-known value of the string tension. However, since we want to compare quenched and unquenched results we need a determination that is applicable in both cases. Since we are calculating matrix elements in the baryon sector it is more appropriate to use the value extracted from the nucleon mass in the chiral limit to set the scale. In the quenched case the value extracted using the nucleon mass is $a^{-1} = 2.04(2)$ GeV ($a = 0.098$ fm) and in the unquenched $a^{-1} = 1.88(7)$ GeV ($a = 0.106$ fm) with a systematic error

TABLE I. κ values and momentum transfers used for the evaluation of the transition form factors. The ratio of the rho mass to the pion mass at these κ values is also given. We used the nucleon mass to set the scale.

Q^2 (GeV^2)					
p at rest	Δ at rest	κ	m_π/m_ρ	m_π (GeV)	No. of Configurations
Quenched: $\beta = 6.0$, $16^3 \times 32$, **q**$^2 = 0.64$ GeV^2					
0.57	0.64	0.1530	0.84	0.877(3)	100
0.55	0.64	0.1540	0.78	0.736(2)	100
0.50	0.64	0.1550	0.70	0.604(2)	100
0.40	0.64	$\kappa_c = 0.1571$	0	0	Extrapolated
Quenched: $\beta = 6.0$, $32^3 \times 64$, **q**$^2 = 0.64$ GeV^2					
0.50	0.64	0.1550	0.69	0.598(4)	100
Quenched: $\beta = 6.0$, $32^3 \times 64$, **q**$^2 = 0.16$ GeV^2					
0.13	0.16	0.1554	0.64	0.537(4)	100
0.10	0.15	0.1558	0.59	0.469(4)	100
0.057	0.13	0.1562	0.50	0.392(4)	100
0.064	0.13	$\kappa_c = 0.1571$	0	0	Extrapolated
Unquenched: $\beta = 5.6$, $16^3 \times 32$, **q**$^2 = 0.54$ GeV^2					
0.48	0.54	0.1560	0.83	0.837(6)	196
0.48	0.54	0.1565	0.81	0.755(10)	200
0.45	0.54	0.1570	0.76	0.655(9)	201
0.45	0.54	0.1575	0.68	0.527(8)	200
0.40	0.53	$\kappa_c = 0.1585$	0	0	Extrapolated

TABLE II. The plateau values of $\mathcal{G}_{M1}^{(a)}$, $\mathcal{G}_{E2}^{(a)}$ in units of $e/2m_N$ and R_{EM} in percent for different fit ranges are given together with the χ^2/DOF for the quenched and SESAM lattices in the rest frame of the Δ. $\mathcal{G}_{C2}^{(a)}$ is also given for the cases where a plateau can be identified. We indicate the value that we adopted with an asterisk.

$16^3 \times 32$ quenched				$16^3 \times 32$ unquenched				$32^3 \times 64$ quenched			
$\kappa = 0.153$				$\kappa = 0.1560$				$\kappa = 0.1554$			
$\mathcal{G}_{M1}$	t_i/a	t_f/a	χ^2/DOF	$\mathcal{G}_{M1}$	t_i/a	t_f/a	χ^2/DOF	$\mathcal{G}_{M1}$	t_i/a	t_f/a	χ^2/DOF
2.25(6)	8	12	0.1	2.35(5)	8	12	0.2	2.98(6)	10	16	1.9
2.25(7)*	8	16	0.2	2.36(5)*	8	16	0.5	3.00(7)	10	20	1.6
2.28(7)	10	12	0.1	2.37(6)	10	12	0.002	3.07(8)	12	16	0.4
2.26(9)	10	16	0.2	2.39(7)	10	16	0.9	3.09(9)*	12	20	0.5
$\mathcal{G}_{E2}$	t_i/a	t_f/a	χ^2/DOF	$\mathcal{G}_{E2}$	t_i/a	t_f/a	χ^2/DOF	$\mathcal{G}_{E2}$	t_i/a	t_f/a	χ^2/DOF
0.036(10)	8	12	0.3	0.004(7)	8	12	2	0.049(15)*	10	16	0.5
0.038(11)*	8	16	0.4	0.003(7)	8	16	1.4	0.046(16)	10	20	1.1
0.037(15)	10	12	0.6	$-0.010(11)$	10	12	1.0	0.047(23)	12	16	0.8
0.042(17)	10	16	0.5	$-0.012(13)$*	10	16	0.5	0.038(26)	12	20	1.2
R_{EM}	t_i/a	t_f/a	χ^2/DOF	R_{EM}	t_i/a	t_f/a	χ^2/DOF	R_{EM}	t_i/a	t_f/a	χ^2/DOF
$-1.6(5)$	8	12	0.3	$-0.12(29)$	8	12	2.0	$-1.6(5)$*	10	16	0.6
$-1.7(5)$*	8	16	0.4	$-0.13(32)$	8	16	1.4	$-1.6(5)$	10	18	1.0
$-1.8(6)$	9	16	0.4	0.01(41)	9	16	1.0	$-1.5(5)$	10	20	1.2
$-1.6(6)$	10	12	0.6	0.44(48)	10	12	1.0	$-1.5(8)$	12	16	0.8
$-1.8(7)$	10	16	0.5	0.52(56)*	10	16	0.5	$-1.2(8)$	12	20	1.3
$\mathcal{G}_{C2}$	t_i/a	t_f/a	χ^2/DOF	$\mathcal{G}_{C2}$	t_i/a	t_f/a	χ^2/DOF	$\mathcal{G}_{C2}$	t_i/a	t_f	χ^2/DOF
								0.18(7)	10	16	0.3
								0.12(13)*	12	16	0.1

$\kappa = 0.155$				$\kappa = 0.1570$				$\kappa = 0.1562$			
$\mathcal{G}_{M1}$	t_i/a	t_f/a	χ^2/DOF	$\mathcal{G}_{M1}$	t_i/a	t_f/a	χ^2/DOF	$\mathcal{G}_{M1}$	t_i/a	t_f/a	χ^2/DOF
1.94(8)	8	12	0.4	1.92(5)	8	12	0.2	2.71(9)	10	16	1.1
1.92(9)	8	16	0.9	1.91(7)*	8	16	0.1	2.72(9)	10	20	1.2
1.95(10)*	9	15	0.8	1.93(8)	9	16	0.3	2.82(13)	12	16	0.2
2.01(12)	10	12	0.02	1.95(9)	10	12	0.2	2.83(13)*	12	18	0.3
1.94(13)	10	16	1.1	1.94(10)	10	16	0.1	2.84(14)	12	20	0.6
$\mathcal{G}_{E2}$	t_i/a	t_f/a	χ^2/DOF	$\mathcal{G}_{E2}$	t_i/a	t_f/a	χ^2/DOF	$\mathcal{G}_{E2}$	t_i/a	t_f/a	χ^2/DOF
0.074(24)	8	12	0.3	0.022(9)	8	12	0.2	0.077(24)*	10	16	0.5
0.072(25)	8	16	0.3	0.023(10)	8	16	0.4	0.075(25)	10	20	0.8
0.078(33)*	9	15	0.3	0.023(13)*	9	15	0.2	0.105(47)	12	16	0.2
0.077(37)	10	12	0.2	0.027(14)	10	12	0.1	0.097(50)	12	18	0.6
0.071(38)	10	16	0.3	0.029(16)	10	16	0.4	0.093(50)	12	20	0.8
R_{EM}	t_i/a	t_f/a	χ^2/DOF	R_{EM}	t_i/a	t_f/a	χ^2/DOF	R_{EM}	t_i/a	t_f/a	χ^2/DOF
$-3.9(1.3)$	8	12	0.2	$-1.1(5)$	8	12	0.2	$-2.9(9)$*	10	16	0.4
$-3.8(1.3)$*	8	16	0.2	$-1.2(5)$	8	16	0.4	$-2.8(10)$	10	20	0.8
$-4.0(1.7)$	9	16	0.2	$-1.2(7)$*	9	16	0.4	$-3.7(1.7)$	12	16	0.3
$-3.8(1.9)$	10	12	0.2	$-1.4(7)$	10	12	0.2	$-3.4(1.7)$	12	18	0.6
$-3.6(1.9)$	10	16	0.2	$-1.5(9)$	10	16	0.4	$-3.2(1.8)$	12	20	0.9
$\mathcal{G}_{C2}$	t_i/a	t_f/a	χ^2/DOF	$\mathcal{G}_{C2}$	t_i/a	t_f/a	χ^2/DOF	$\mathcal{G}_{C2}$	t_i/a	t_f/a	χ^2/DOF
				0.11(3)	8	12	0.2	0.25(9)	10	15	0.2
				0.11(3)*	8	15	0.3				
				0.12(5)	10	12	0.4	0.17(21)*	12	15	0.1
				0.13(5)	10	15	0.3				

of about 15% [11] coming from the choice of the chiral extrapolation *Ansatz*. We note that if one uses the rho mass at the chiral limit one obtains $a^{-1} = 2.3$ GeV ($a = 0.087$ fm) for both the quenched and the unquenched theory [11,19,20], with a systematic error of about 10% due to the choice of fitting range and chiral extrapolation ansatz [19]. Therefore using the nucleon or the rho mass to set the scale yields results for a within the systematic uncertainties. We would
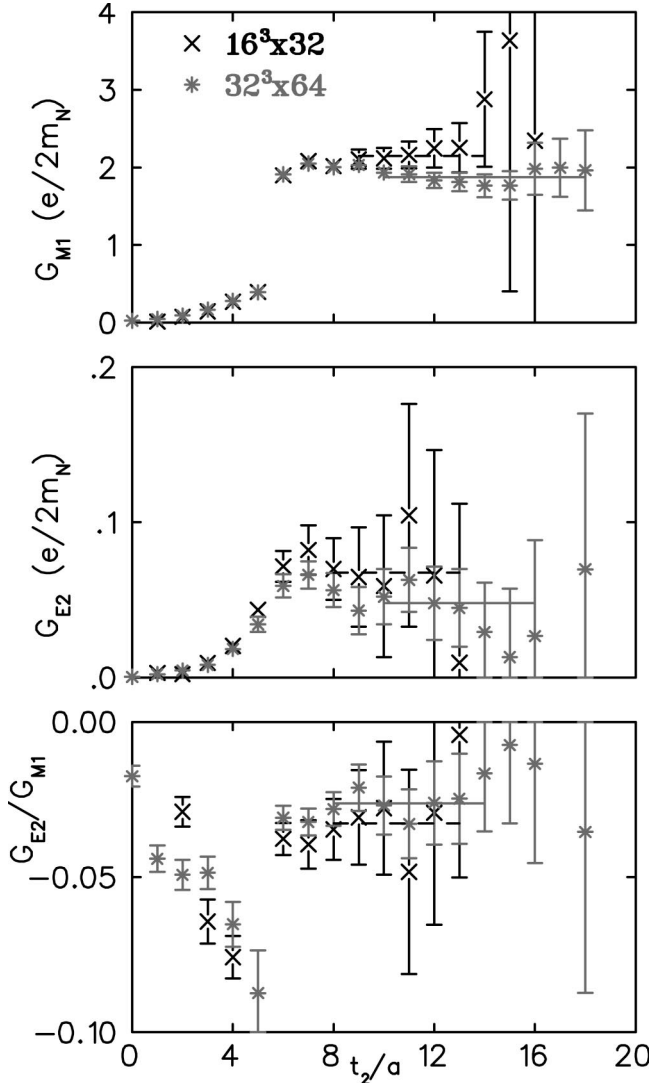
FIG. 9. $\mathcal{G}_{M1}^{(a)}$, $\mathcal{G}_{E2}^{(a)}$ in units of natural magnetons and $-\mathcal{G}_{E2}^{(a)}/\mathcal{G}_{M1}^{(a)}$ in the quenched theory for lattices of size $16^3 \times 32$ ($\times$ symbols) and $32^3 \times 64$ (stars) at $\kappa = 0.155$ and momentum transfer $\mathbf{q} = (2\pi/16a,0,0)$. For this comparison the data for the large lattice are shifted by two time slices to the left so that the coupling of the photon to the quark occurs at the same time point on the graph. The dashed and solid lines are the plateau values for the small and larger lattices, respectively.

like to stress here that in the ratios R_{EM} and R_{SM}, which are the experimentally measured quantities, the lattice spacing does not explicitly enter and therefore a precise determination of a is less crucial here than in other studies. In Table I we use the value for a obtained from the nucleon mass to convert the momentum transfer $\mathbf{q}$ at which the transition moments are evaluated to physical units. The lattice four-momentum transfer Q^2 depends on the κ values through the nucleon and Δ masses. These values are given in Table I. As already mentioned we consider two kinematically different cases, one with the Δ being at rest and the other with the nucleon at rest. For all κ values, including κ_c, for the case when the Δ is produced at rest the variation in Q^2 is negligible. For the case when the nucleon is at rest the variation in
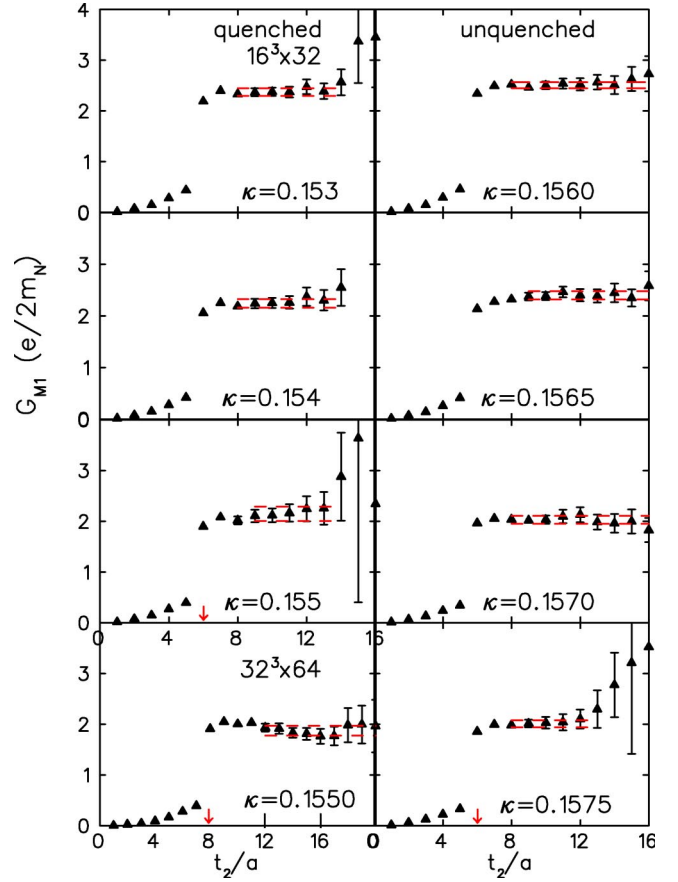

FIG. 10. $\mathcal{G}_{M1}^{(a)}$ at momentum transfer $\mathbf{q} = (2\pi/16a,0,0)$ in the rest frame of the nucleon. The three upper graphs on the left show the quenched results for the lattice of size $16^3 \times 32$ at $\kappa = 0.153$, 0.154, and 0.155. The lowest graph on the left shows quenched results for the lattice of size $32^3 \times 64$. On the right we show the unquenched results at $\kappa = 0.1560$, 0.1565, 0.1570, and 0.1575. The photon couples to the quark at $t_1/a = 6$ for the small lattices and at $t_1/a = 8$ for the large lattice as shown by the arrow. The dashed lines show the fit range and bounds on the plateau value obtained by jackknife analysis.

Q^2 over the range of κ values considered here is sizable, in particular when $\mathbf{q} = (2\pi/32a,0,0)$ where Q^2 changes by a factor of 2. We will come back to this point in Sec. IV when we discuss the chiral extrapolation of the results. In all the evaluations we take u and d quarks of the same mass. The current couples to the quark at time slice $t_1 = 6a$ for the lattices of size $16^3 \times 32$ and at $t_1 = 8a$ for the lattice of size $32^3 \times 64$.

To extract a reliable value for the form factors we identify the best plateau region having the largest possible range and ensure that changing the fit range within this plateau region produces results that remain within statistical errors of each other. In Table II we give the variation of the mean values from changing the fit range of the plateaus for two representative κ values for each lattice in the rest frame of the Δ. The quality of the plateaus and best fit ranges for the case when the nucleon is at rest is displayed in Figs. 10 and 11 for $\mathcal{G}_{M1}$ and in Fig. 12 for $\mathcal{G}_{E2}$. In Fig. 13 we display the plateaus for
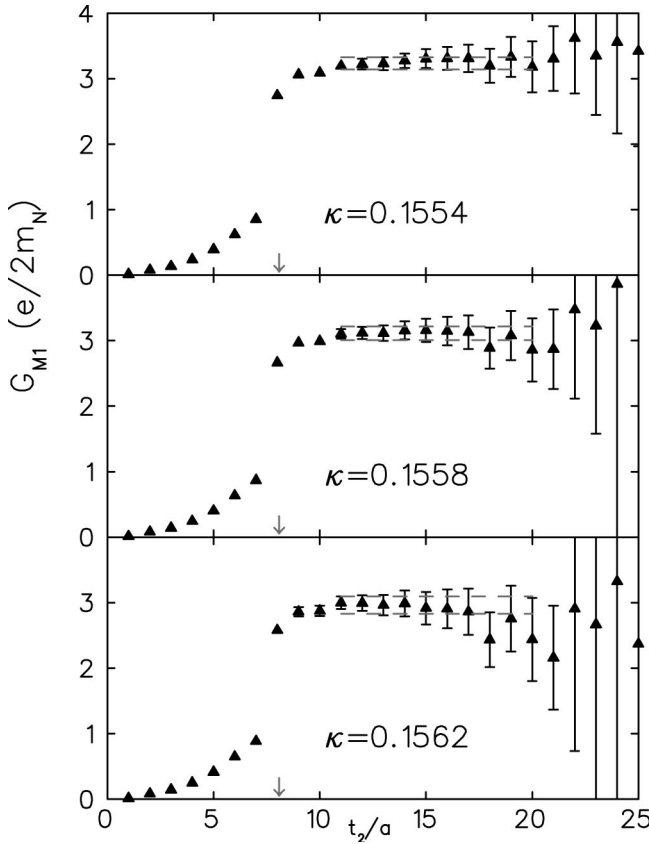
FIG. 11. $\mathcal{G}_{M1}^{(a)}$ for the quenched theory on a lattice of size $32^3 \times 64$ at $\kappa = 0.1554$, 0.1558, and 0.1562 with the nucleon at rest and for momentum transfer $\mathbf{q} = 2\pi/32a$. The photon couples to the quark at $t_1/a = 8$ as indicated by the arrow. The dashed lines show the fit range and bounds on the plateau value obtained by jackknife analysis.

FIG. 12. $\mathcal{G}_{E2}^{(a)}$. The notation is as in Fig. 10.

the large quenched lattice for $\mathcal{G}_{E2}$ in the rest frame of the Δ in order to have one case of direct comparison to the numbers chosen for the best plateau in Table II. In Fig. 14 we show the plateaus and best fit ranges for R_{EM} in the rest frame of the nucleon. From the plateau values given in Table II it can be seen that the dependence of the results on the fit ranges is, in all cases, well within the statistical errors obtained from jackknife analysis.

In order to access finite volume effects we calculate the transition form factors in the quenched theory on two lattices of size $16^3 \times 32$ and $32^3 \times 64$ at the same momentum transfer. We show the results for $\mathcal{G}_{M1}$, $\mathcal{G}_{E2}$, and the ratio $\mathcal{G}_{E2}/\mathcal{G}_{M1}$ in Fig. 9. The data for $\mathcal{G}_{M1}$ obtained on the large volume lie systematically below the ones obtained on the small lattice. The results for $\mathcal{G}_{E2}$ as well as for the ratio $\mathcal{G}_{E2}/\mathcal{G}_{M1}$ have overlapping errors. On the two volumes, the difference in the plateau values is smallest in the ratio since volume effects tend to cancel in numerator and denominator. The plateau values for $\mathcal{G}_{M1}$ given in Table III are systematically lower by 10–15 % on the larger lattice. Therefore there is a volume correction to the results obtained on the small lattices of the order of 10%, which is comparable to the statistical error. The results obtained on the larger lattice have negligible volume dependence if the volume correction scales in inverse
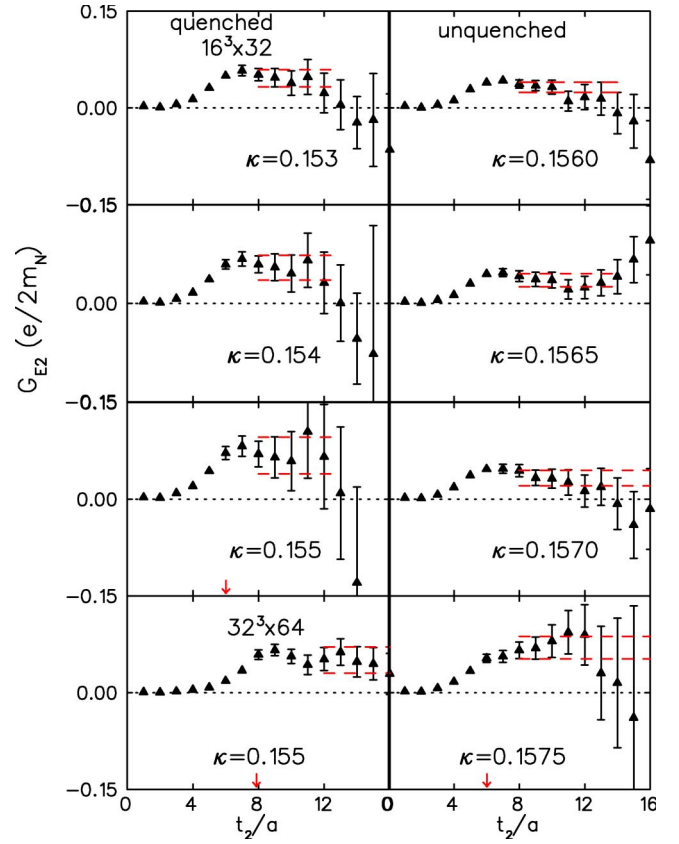
proportion to the volume. For $\mathcal{G}_{E2}$ and the ratio $\mathcal{G}_E/\mathcal{G}_{M1}$, which carry larger statistical errors, the volume dependence is harder to access since the difference in the values for the two volumes is well within the statistical errors.

The values for $\mathcal{G}_{M1}$ extracted from the fits to the plateaus are collected in Table III. The overall quality of the plateaus as well as the best fit range chosen for each κ value can be seen in Fig. 10 for $\mathbf{q} = (2\pi/16a,0,0)$ and in Fig. 11 for $\mathbf{q} = (2\pi/32a,0,0)$ for both the quenched and the unquenched theory. The larger time extension of the lattice improves the identification of the plateau region, yielding reliable results for $\mathcal{G}_{M1}$ at the lighter quark masses. From the values given in Table III we conclude that, when the Δ is produced at rest, the definitions $\mathcal{G}_{M1}^{(a)}$ or $\mathcal{G}_{M1}^{(b)}$ yield the same values. The case where the Δ carries momentum $\mathbf{q}$ along the x direction $\mathcal{G}_{M1}^{(b)}$, which is extracted from matrix elements for which the Δ vector index is in the x direction, yields consistently larger values than those obtained from $\mathcal{G}_{M1}^{(a)}$. This difference in the values of $\mathcal{G}_{M1}^{(a)}$ and $\mathcal{G}_{M1}^{(b)}$ is volume independent and increases from about 6% for the heavier quarks to about 15% for the lighter ones. It is also independent of the value of the momentum carried by the Δ. It would be interesting to allow momentum transfers in all directions to check if this difference will be reduced and also use an $\mathcal{O}(a)$ improved Dirac operator to check whether it is due to finite a effects.

To look for sea quark effects on the value of $\mathcal{G}_{M1}$ we compare the quenched results on the small lattice to the unquenched results using the SESAM configurations at a simi-
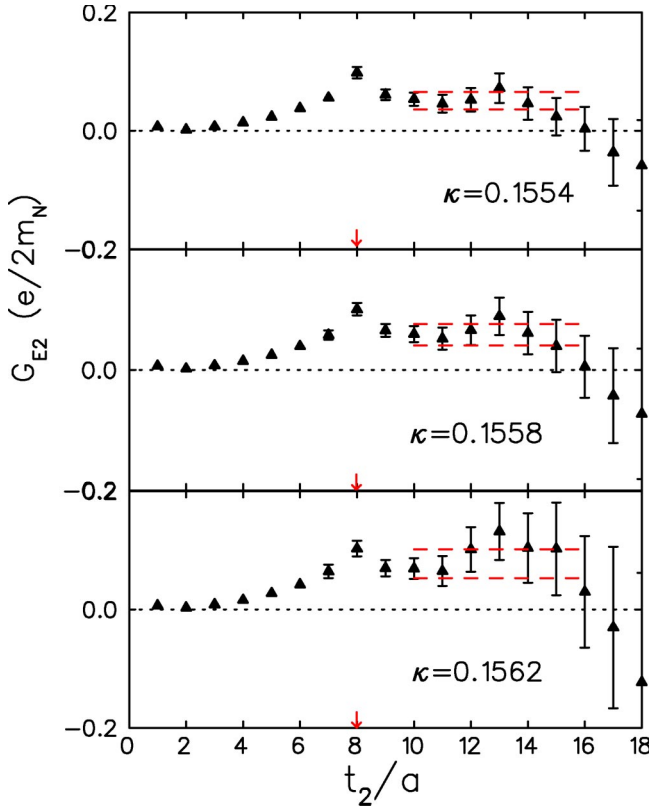
FIG. 13. $\mathcal{G}_{E2}^{(a)}$ for Δ at rest. The notation is as in Fig. 11.
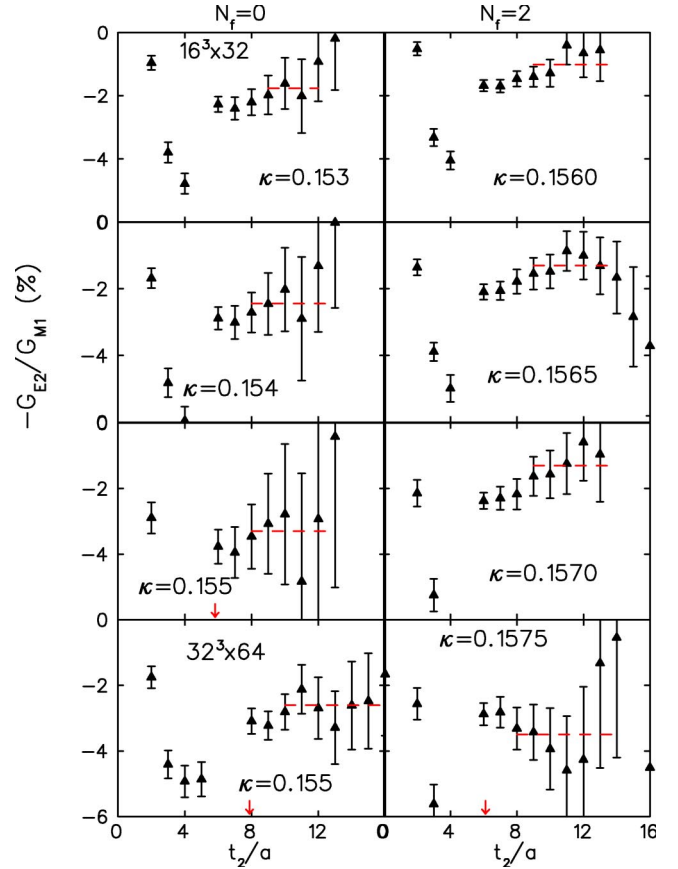

FIG. 14. The ratio $-\mathcal{G}_{E2}^{(a)}/\mathcal{G}_{M1}^{(a)}$ in the lab frame of the nucleon. The three upper graphs on the left show results for the quenched theory on a lattice of size $16^3 \times 32$ for $\mathbf{q} = (2\pi/16a,0,0)$ at $\kappa = 0.153$, 0.154, 0.155 and the lowest shows results for a lattice of size $32^3 \times 64$ for the same value of $\mathbf{q}$ at $\kappa = 0.155$. On the right we show results for the SESAM configurations at $\kappa = 0.1560$, 0.1565, 0.1570, and 0.1575 for $\mathbf{q} = (2\pi/16a,0,0)$. The current couples to the quark at time $t_1/a = 6$ for the lattices of temporal size $32a$ and at $t_1/a = 8$ for the lattice of temporal size $64a$, as shown by the arrow.

lar ratio of the pion mass to the rho mass. From the values of pion to rho mass ratios given in Table I one thus compares quenched results at $\kappa = 0.153$, 0.154, and 0.155 to the unquenched results at $\kappa = 0.1560$, 0.1570, and 0.1575, respectively. Unquenching leads to a stronger quark mass dependence, increasing the value of $\mathcal{G}_{M1}$ at the heaviest quark mass and reducing it at the two lighter quark masses.

In Fig. 12 we show the quenched and unquenched results for $\mathcal{G}_{E2}^{(a)}$ at $\mathbf{q} = (2\pi/16a,0,0)$ in the lab frame of the nucleon. The plateau region is limited to a few time slices for the quenched lattice, whereas for the SESAM lattice for twice the statistics the fits can be extended over a larger time interval. For a static Δ both $\mathcal{G}_{E2}^{(a)}$ and $\mathcal{G}_{E2}^{(b)}$ show a similar behavior and the best plateau fit ranges are given, for $\mathcal{G}_{E2}^{(a)}$, in Table II for representative κ values. As we already mentioned, although the central value for $\mathcal{G}_{E2}$ decreases on going to the larger lattice, the observed decrease is well within our statistics. Similarly, unquenching systematically reduces the value of $\mathcal{G}_{E2}$. However, with our statistics this reduction remains within errors, for the three κ values that correspond to similar ratios of pion to rho mass. Plateau identification improves for the large lattice as seen in Fig. 12, where we display results at $\kappa = 0.155$ for both the large and small quenched lattices at equal momentum transfer. This improvement is also seen in Fig. 13, where we show results for the large quenched lattice at $\mathbf{q} = (2\pi/32a,0,0)$, even though lighter quarks are used. Here part of the noise reduction is due to having a smaller value of the momentum transfer. This enables us to check the stability of our fits by changing the fit range as given in Table II.

Our lattice results for the ratio $-\mathcal{G}_{E2}^{(a)}/\mathcal{G}_{M1}^{(a)}$ are displayed for the quenched and the unquenched theory in Fig. 14 in the rest frame of the nucleon. The general trend is that this ratio becomes more negative as we approach the chiral limit. The plateau values seen in the figure and given in Table III give no indication of an increase in this ratio as we unquench. This may mean that pion cloud contributions, expected to drive this ratio more negative, are suppressed at these large quark masses. However, one must keep in mind that part of the pion cloud is taken into account in the quenched theory since using relativistic quarks includes backward propagation in time and thus effectively pionic contributions. A study with lighter pions is required in order to assess the importance of pion contributions due to sea quarks on the value of this ratio and thus on nucleon deformation.

Finally, in Fig. 15 we show the results for $\mathcal{G}_{C2}^{(a)}$ with Δ static for the large quenched lattice for which the ratio R_σ can be obtained for long enough time separations $t_2 - t_1$ to allow plateau identification. Although an evaluation of $\mathcal{G}_{C2}^{(a)}$ is also carried out for the SESAM configurations, a large

TABLE III. Results for $\mathcal{G}_{M1}$, $\mathcal{G}_{E2}$ in units of natural magnetons ($e/2m_N$) and for the ratio $-\mathcal{G}_{E2}/\mathcal{G}_{M1}$.

	p at rest		Δ at rest		p at rest	Δ at rest		p at rest	Δ at rest	Δ at rest
κ	$\mathcal{G}_{M1}^{(a)}$	$\mathcal{G}_{M1}^{(b)}$	$\mathcal{G}_{M1}^{(a)}$	$\mathcal{G}_{M1}^{(b)}$	$\mathcal{G}_{E2}^{(a)}$	$\mathcal{G}_{E2}^{(a)}$	$\mathcal{G}_{E2}^{(b)}$	R_{EM} (%)		$\mathcal{G}_{C2}^{(a)}$
					Quenched: $\beta=6.0$, $16^3\times32$, $\mathbf{q}=(2\pi/16a,0,0)$					
0.153	2.37(7)	2.52(7)	2.25(7)	2.26(7)	0.046(13)	0.038(11)	0.035(12)	$-1.8(8)$	$-1.7(5)$	
0.154	2.24(8)	2.41(9)	2.12(8)	2.14(8)	0.054(19)	0.054(19)	0.045(18)	$-2.4(9)$	$-2.3(7)$	
0.155	2.15(14)	2.27(11)	1.95(10)	1.99(10)	0.068(28)	0.078(33)	0.071(24)	$-3.3(1.4)$	$-3.8(1.3)$	
					Quenched: $\beta=6.0$, $32^3\times64$, $\mathbf{q}=(2\pi/16a,0,0)$					
0.1550	1.87(10)	1.99(10)	1.78(7)	1.76(7)	0.048(20)	0.049(40)	0.056(41)	$-2.6(7)$	$-0.95(48)$	
					Quenched: $\beta=6.0$, $32^3\times64$, $\mathbf{q}=(2\pi/32a,0,0)$					
0.1554	3.24(10)	3.44(10)	3.09(9)	3.12(9)	0.073(30)	0.049(15)	0.049(16)	$-2.2(9)$	$-1.6(5)$	0.12(13)
0.1558	3.11(11)	3.35(10)	2.97(11)	3.00(11)	0.079(23)	0.059(18)	0.057(18)	$-3.0(1.2)$	$-2.1(6)$	0.12(15)
0.1562	2.96(13)	3.22(12)	2.83(13)	2.84(14)	0.131(53)	0.077(24)	0.075(24)	$-4.1(2.0)$	$-2.9(9)$	0.17(21)
					$N_f=2$: $\beta=5.6$,$16^3\times32$, $\mathbf{q}=(2\pi/16a,0,0)$					
0.1560	2.51(6)	2.65(6)	2.36(5)	2.36(5)	0.031(8)	$-0.012(13)$	$-0.011(12)$	$-1.1(4)$	0.52(56)	—
0.1565	2.34(8)	2.52(7)	2.13(6)	2.15(6)	0.035(10)	0.020(11)	0.025(9)	$-1.3(5)$	$-0.7(5)$	0.11(3)
0.1570	2.03(8)	2.18(9)	1.91(7)	1.90(7)	0.033(12)	0.023(13)	0.027(10)	$-1.3(7)$	$-1.2(7)$	0.11(3)
0.1575	2.01(7)	2.29(8)	1.73(6)	1.72(7)	0.070(17)	0.021(16)	0.025(16)	$-3.5(9)$	$-1.2(9)$	0.08(3)

enough plateau range could not be identified for all κ values. Poor plateau identification leading to a limited fit range may introduce systematic errors that are not included in the errors of the extracted values given in Table III. However, for the cases where we can fit over four time slices far enough from the time of the current insertion the mean value of $\mathcal{G}_{C2}^{(a)}$ is positive at all κ values. Therefore, even though the systematic errors are largest for this form factor, which means that the jackknife errors given in Table III provide an underestimation of the actual error, our lattice results favor a negative value for the ratio $-\mathcal{G}_{C2}/\mathcal{G}_{M1}$ in agreement with experiment.

IV. CHIRAL EXTRAPOLATIONS

In order to obtain physical results we need to extrapolate the lattice data to the chiral limit. Chiral perturbation theory has been applied to calculate the transition form factors [13] but the range of validity is limited to very small quark masses and very low momentum transfers and therefore it cannot be used in the current analysis.[1] Since the nucleon or the Δ carry a finite momentum we expect chiral logs that appear at next-to-leading order in chiral perturbation theory to be suppressed for the momentum transfers studied in this work. Therefore a behavior proportional to the pion mass squared should be appropriate all the way to very near the chiral limit. The linear dependence of our results on the pion mass m_π squared is seen from Figs. 16, 17, and 18. The results shown in these figures are for the kinematical case where the Δ is stationary and Q^2 remains almost unchanged as the pion mass approaches the chiral limit. The errors on the lattice data are obtained by jackknife analysis and are purely statistical. Given the fact that we have results only at three values of κ in the quenched case and four in the unquenched case a linear fit is the best option we have. For the quenched calculation the error on the extrapolated value at the chiral limit that we quote in Table IV is obtained by doing a complete jackknife analysis for the three κ values. In
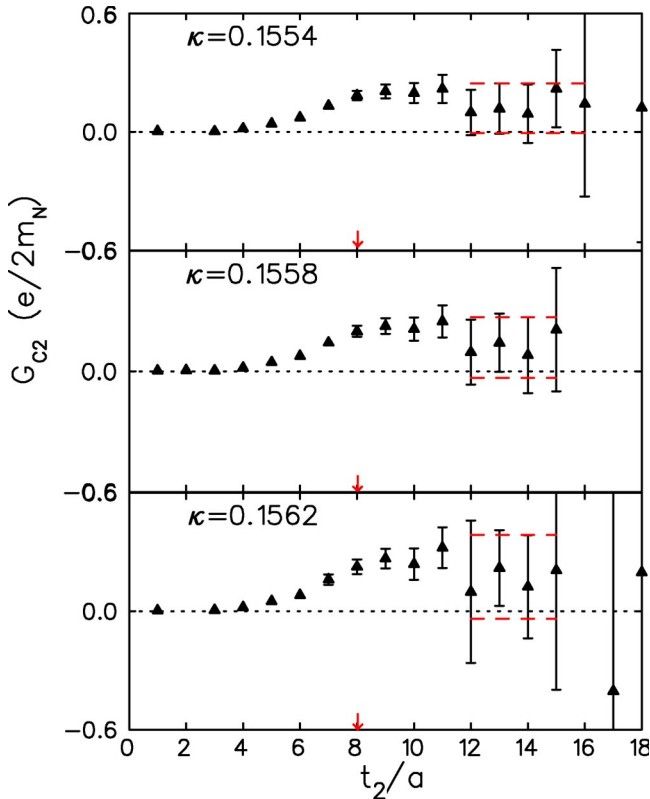

FIG. 15. $\mathcal{G}_{C2}^{(a)}$ in the rest frame of the Δ. The notation is as in Fig. 11.

---

[1]After the completion of this work, chiral perturbation theory was also applied in the quenched case up to next to leading order by Arndt and Tiburzi [25]. The main conclusion of this work is that $\mathcal{G}_{M1}$ and $\mathcal{G}_{E2}$ depend logarithmically on the pion mass squared, as in the full theory.
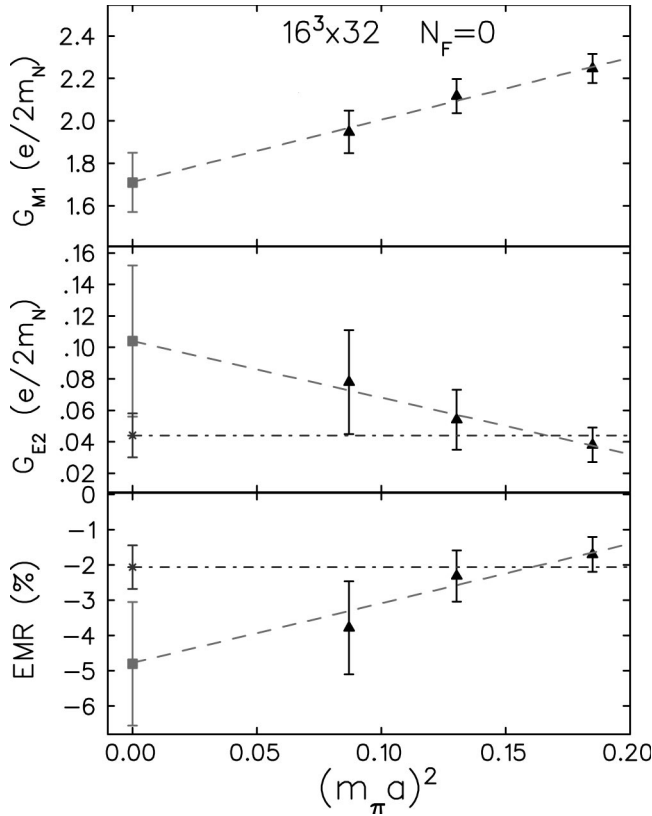
FIG. 16. Top, $\mathcal{G}_{M1}^{(a)}$; middle, $\mathcal{G}_{E2}^{(a)}$; and bottom, EMR in % versus m_π^2 in lattice units in the rest frame of the Δ for the quenched $16^3 \times 32$ lattice. The dashed line is fitted to $a + b m_\pi^2$ and the dash-dotted line to a constant with the chiral value obtained shown with a filled square and star for the two *Ansätze*, respectively.

the unquenched case, configurations at each quark mass are obtained from different Monte Carlo simulations, and a standard χ^2-minimization procedure, which assumes uncorrelated data points at each quark mass, can be applied.

Extrapolating linearly in m_π^2, we obtain for both quenched and unquenched lattices very good fits for $\mathcal{G}_{M1}$, which is the most accurately determined quantity. All the data points fall nicely on a straight line even in the unquenched case, where the data at different quark masses are uncorrelated since they are obtained using a different set of configurations. A linear *Ansatz* also fits well the quenched results for $\mathcal{G}_{E2}$ and R_{EM} as can be seen in Figs. 16, 17, and 18. For the corresponding unquenched results, although a linear *Ansatz* still provides a good fit, giving a χ^2 per degree of freedom=1.1 for $\mathcal{G}_{E2}$ and $\chi^2/\text{DOF}=0.6$ for R_{EM}, the unquenched results for $\mathcal{G}_{E2}$ and R_{EM} show very weak mass dependence at the three lightest quark masses. Chiral perturbation theory suggests a similar mass dependence for $\mathcal{G}_{E2}$ as that for $\mathcal{G}_{M1}$. An unquenched calculation with higher statistics on a larger lattice to avoid finite size effects that, especially at the lightest quark mass ($\kappa = 0.1575$), can be significant is called for to check this mass dependence. Given this weak mass dependence, we also fit $\mathcal{G}_{E2}$ and R_{EM} to a constant which gives a lower value for $\mathcal{G}_{E2}$ and the absolute magnitude of R_{EM} at the chiral limit. For comparison we include also for the quenched results the value obtained us-
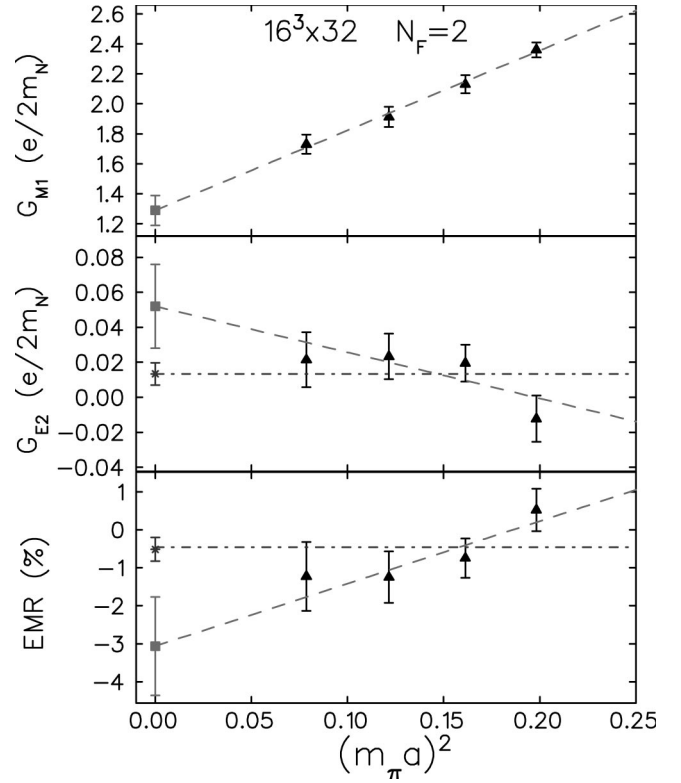

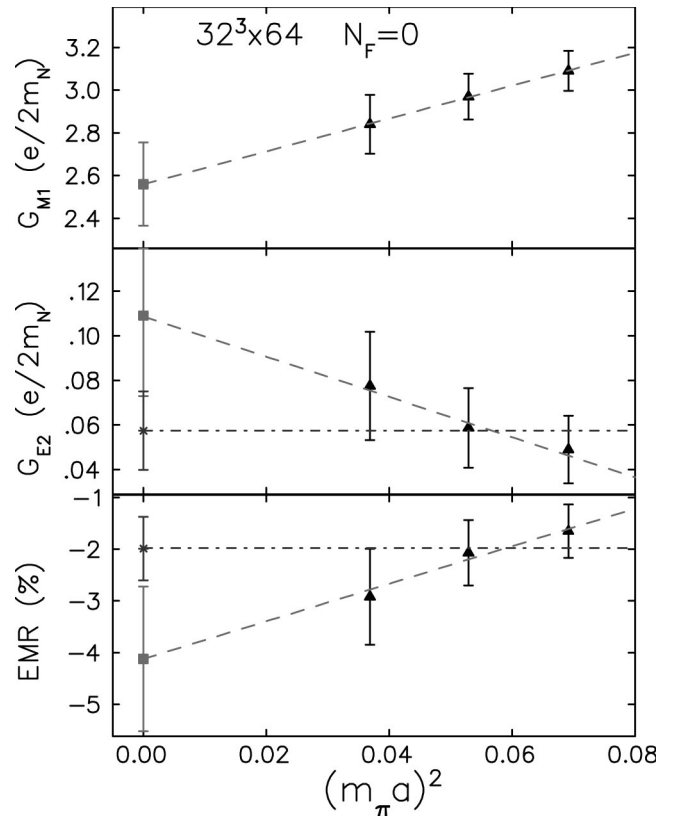FIG. 17. The same as in Fig. 16 but for the unquenched theory.

FIG. 18. The same as in Fig. 16 but for the quenched $32^3 \times 64$ lattice.

TABLE IV. Results for $\mathcal{G}_{M1}$, $\mathcal{G}_{E2}$ in units of $e/2m_N$ and for the ratio $R_{EM} = -\mathcal{G}_{E2}/\mathcal{G}_{M1}$ in percent extrapolated to the chiral limit. All errors given are statistical. The last column gives the prediction for R_{EM} in percent obtained within the SL model [21] where for the quenched case we quote their values without pion cloud contributions and for the unquenched theory we give their fully dressed results for the case where the Δ is produced at rest. In the last two columns we give the experimental results at similar values of Q^2.

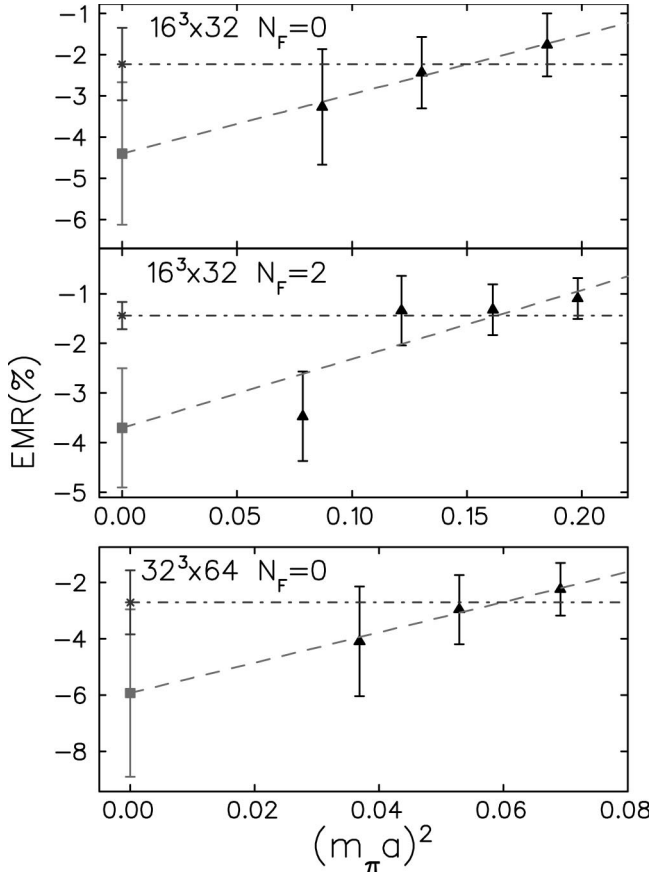|	Q^2 (GeV^2)	$\mathcal{G}_{M1}^{(a)}$	$\mathcal{G}_{E2}^{(a)}$	R_{EM}	
		Quenched QCD			SL
p at rest	0.40			$-4.4(1.7)$	
Δ at rest	0.64	1.71(14)	0.104(48)	$-4.8(1.8)$	-1.3
Δ at rest	0.13	2.56(20)	0.108(36)	$-4.1(1.4)$	-1.3
p at rest	0.06			$-5.9(3.0)$	
		Unquenched QCD			SL
Δ at rest	0.53	1.29(10)	0.052(24)	$-3.1(1.3)$	-2.7
p at rest	0.40			$-3.7(1.2)$	
		Experimental results			
	0.126			$-2.0(2)(2.0)$ [1]	
	0.40			$-3.4(4)(4)$ [2]	
	0.52			$-1.6(4)(4)$ [2]	

FIG. 19. The EMR ratio in % in the rest frame of the nucleon. Top for the quenched $16^3 \times 32$ lattice, middle for the unquenched theory, and bottom for the quenched $32^3 \times 64$ lattice. The dashed line is fitted to $a + bm_\pi^2$ and the dash-dotted line to a constant with the chiral value obtained shown with a filled square and star for the two *Ansätze*, respectively.
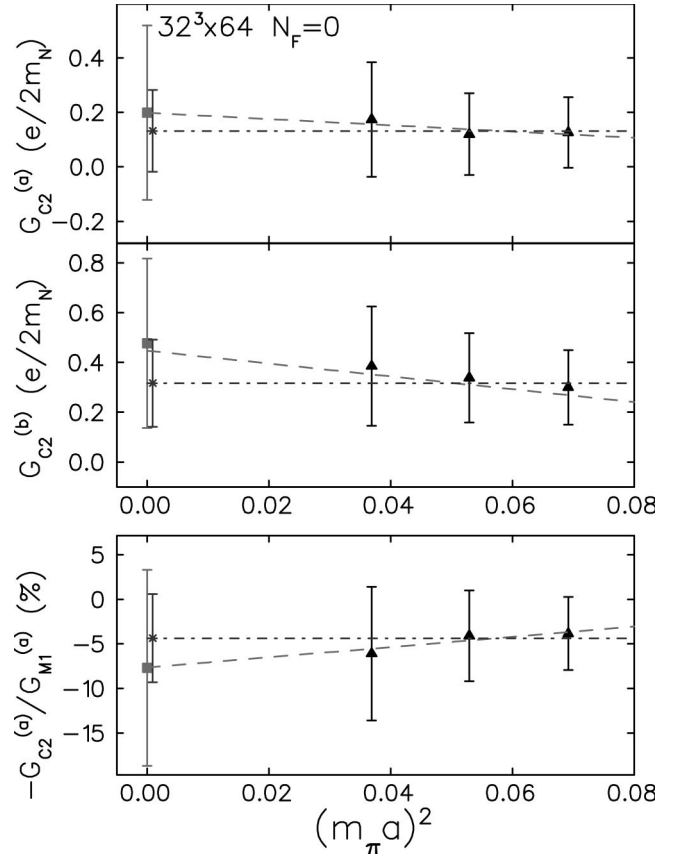
FIG. 20. Top, $\mathcal{G}_{C2}^{(a)}$; middle, $\mathcal{G}_{C2}^{(b)}$; and bottom, $-\mathcal{G}_{C2}^{(a)}/\mathcal{G}_{M1}^{(a)}$ in % versus m_π^2 in lattice units in the rest frame of the Δ for the quenched $32^3 \times 64$ lattice. The dashed line is fitted to $a + bm_\pi^2$ and the dash-dotted line to a constant with the chiral value obtained shown with a filled square and star for the two *Ansätze*, respectively.

ing a constant fit even though a linear fit in m_π^2 is favored by the data. Although the chiral absolute value of R_{EM} is reduced by modifying the fitting *Ansatz* to a constant, R_{EM} remains negative in all cases.

For kinematics where the nucleon is at rest Q^2 changes as we approach the chiral limit. This change is particularly severe for the large quenched lattice where one would need the extrapolation of form factors computed at Q^2 that decrease by 50%. In phenomenological studies one models the Q^2 dependence of the three form factors by

$$\mathcal{G}_a(Q^2) = \mathcal{G}_a(0) R_a(Q^2) G_E^p(Q^2), \qquad (33)$$

where $R_a(Q^2)$ for $a = M1, E2$, and $C2$ measures the deviations from the proton electric form factor $G_E^p(Q^2) = 1/(1 + Q^2/0.71)^2$. Usually experimental data are fitted by taking $R_{M1}(Q^2) = R_{E2}(Q^2) = R_{C2}(Q^2) = 1 + \alpha \exp(-Q^2\gamma)$ [21]. There are not enough data to simultaneously fit the Q^2 and the quark mass dependence. We are in the process of studying the Q^2 dependence of these form factors using the fixed source sequential technique [22,23]. However, assuming that the above phenomenological *Ansätze* provide a good description for the Q^2 dependence of $\mathcal{G}_{M1}$ and $\mathcal{G}_{E2}$, we expect the Q^2 dependence to cancel in the ratio R_{EM}. Therefore a chiral extrapolation can be performed for R_{EM} also in the case of the nucleon being at rest. A constant and a linear fit in m_π^2 are shown for the three lattices in Fig. 19. Once more the constant provides a lower limit for the absolute magnitude of R_{EM} and still leads to a negative value in the chiral limit in all cases.

Finally, we cannot observe any quark mass dependence for $\mathcal{G}_{C2}^{(a)}$ and $\mathcal{G}_{C2}^{(b)}$ as well as for the ratio $-\mathcal{G}_{C2}^{(a)}/\mathcal{G}_{M1}^{(a)}$ given the present statistical uncertainties as can be seen in Fig. 20. We included in the figure a constant and a linear fit yielding results that are consistent with each other. We show only results obtained in the rest frame of the Δ for the large quenched lattice where we have the best signal. For this lattice and kinematics at $Q^2 = 0.13$ GeV^2 the values we extract from the linear *Ansatz* are $\mathcal{G}_{C2}^{(a)} = 0.20(32)$ and $\mathcal{G}_{C2}^{(b)} = 0.48(34)$ in units of natural magnetons $(e/2m_N)$. Changing the fitting range can lead to changes of the mean value of about 30% at each κ value. Although the mean values of $\mathcal{G}_{C2}^{(b)}$ are systematically larger than those of $\mathcal{G}_{C2}^{(a)}$ at all κ values they are always within statistical errors. Despite the large statistical and systematic uncertainties on this quantity, the data favor more a negative than a positive CMR ratio.

V. DISCUSSION

In Table IV we list the chiral extrapolated values of the $M1$ and $E2$ form factors obtained in the rest frame of the Δ

as well as of the ratio R_{EM} obtained for both kinematics. The values given are the result of using a linear *Ansatz* in m_π^2 to extrapolate to the chiral limit, and the quoted errors are only statistical. As discussed in Secs. III and IV there are a number of systematic errors that we must consider when comparing the results of Table IV to the experimental ones. We summarize here the source of systematic errors on the form factors and their ratios. Finite volume effects are estimated by performing a quenched calculation at the same value of momentum transfer on a lattice of size $16^3 \times 32$ and $32^3 \times 64$ at $\beta = 6.0$. Assuming a 1/volume dependence for $\mathcal{G}_{M1}$ the results show a 10–15 % correction for the data obtained on the small lattice and negligible for the larger lattice. The statistical errors on $\mathcal{G}_{E2}$ are too large to enable any volume correction to be extracted. However, one would expect a similar volume dependence as for $\mathcal{G}_{M1}$. On the other hand the volume dependence largely cancels in the ratio and so we expect both EMR and CMR ratios to have negligible volume dependence. The variation in the mean values obtained by varying the plateau ranges is smaller as compared to the statistical errors as can be seen from Table II, where we have given the values obtained using different fit ranges for representative κ values for all the lattices studied in this work. We look for unquenching effects by comparing quenched and unquenched results on lattices of similar physical volume and lattice spacing as well as the pion to rho mass ratio. For pion masses in the range of 800–500 MeV unquenching effects are within statistical errors. Extrapolation of the lattice results to the chiral limit represents the biggest uncertainty that can be eliminated only by evaluating the form factors closer to the chiral limit. Avoiding any chiral extrapolations the results on the two quenched and on the unquenched lattices at the lightest quark mass give a ratio R_{EM} in the range of about $(-1$ to $-5)\%$, which is in accord with the range obtained in experimental measurements. Both quenched and unquenched calculations are done at values of β corresponding to a lattice spacing of about 0.1 fm. Estimating finite lattice spacing effects would require repeating the calculation at two larger values of β, keeping the physical volume constant and attempting a continuum extrapolation. This is beyond our current computer resources and no systematic error due to the finite lattice spacing can be estimated.

In the last column of Table IV we give the results for the ratio R_{EM} obtained in the Sato-Lee (SL) model using an effective Hamiltonian defined in the subspace of $\pi N \oplus \gamma N \oplus \Delta$ [21]. Within the SL model R_{EM} is calculated in the rest frame of the Δ as a function of Q^2 for bare and dressed vertices. It is interesting that for bare vertices these authors obtain nonzero values for R_{EM} pointing to the fact that a

TABLE V. f_{M1}, f_{E2}, $A_{1/2}$, and $A_{3/2}$ in units of GeV$^{-1/2}$.

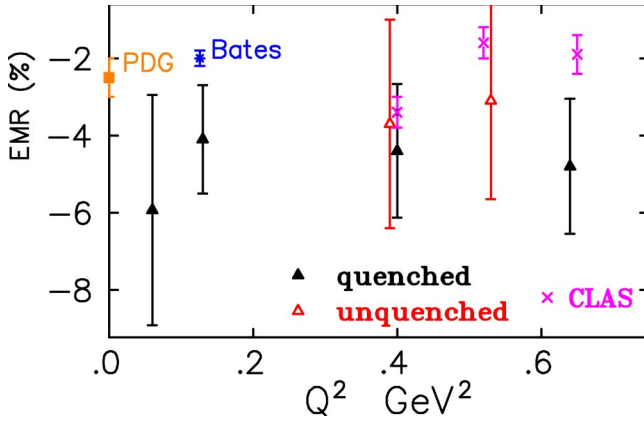| Lattice	$-q^2$ (GeV^2)	f_{M1}	f_{E2}	$A_{1/2}$	$A_{3/2}$
$16^3 \times 32$	0.64	0.266(22)	$-0.016(7)$	$-0.109(13)$	$-0.244(20)$
$32^3 \times 64$	0.13	0.296(23)	$-0.012(4)$	$-0.129(12)$	$-0.267(20)$
SESAM	0.53	0.194(15)	$-0.0078(36)$	$-0.085(8)$	$-0.175(13)$

FIG. 21. The ratio R_{EM} in % versus Q^2 at the chiral limit. Filled triangles are quenched and open triangles are unquenched results. The filled square is the Particle Data Group result at $Q^2=0$ [24], the crosses are from Ref. [2], and the star is from Ref. [1]. The errors shown on the experimental results are statistical. The lattice values shown are those obtained using a linear fit in m_π^2 to extrapolate to the chiral limit. In the unquenched case the error bars are increased so that an extrapolation to the chiral limit using a constant lies within the shown error bands.

nonzero electric quadrupole amplitude implying nucleon deformation that obtained even without pions. This is in agreement with lattice results on the rho deformation that is observed in the quenched approximation without pion contributions [5]. Comparing the value obtained in the SL model at $Q^2=0.64$ GeV^2 and 0.13 GeV^2 using bare vertices to our quenched lattice result via Eq. (5) [21], we see that quenched QCD produces a more negative value for R_{EM} than that obtained in the SL model. One must, however, take into account that, in the baryonic sector, quenching still includes part of the pion cloud due to quarks propagating backwards in time. These are absent in the SL model with bare vertices. On the other hand unquenched lattice results at quark masses that correspond to pion masses in the range 500–800 MeV do not influence the value of R_{EM}. This implies that pion cloud contributions from sea quarks at these pion masses are not large. It remains an open issue whether this means that pionic contributions from back-going quarks are also small, in which case the difference between quenched lattice and SL model results cannot be explained solely by pion contributions from back-going quarks. Results for R_{EM} obtained in the SL model with fully dressed vertices are twice as negative as those obtained with bare vertices, showing, within this model, the importance of pionic contributions to deformation. Our unquenched results, obtained here for rather heavy pions, show no significant enhancement which may reflect that $q\bar{q}$ creation is suppressed. Since it is for light pions that large pionic contributions are expected, it is imperative to repeat the calculation with dynamical quarks closer to the chiral limit to study sea quark contributions.

The values of the ratio R_{EM} given in Table IV can be compared to those measured at various values of Q^2 in recent experimental searches for nucleon deformation. The lattice results for R_{EM} are plotted in Fig. 21 together with the recently measured experimental data. In the figure we also

included the Particle Data group value for R_{EM} at $Q^2=0$ [24]. Once more what can be seen from this figure is that quenched and unquenched results are within errors. The unquenched results at our two available momentum transfers are in agreement with the experimental results. We stress that all the errors shown on this figure are statistical. For the experimental results the systematic error is about the same as the statistical error. For the lattice results the most severe systematic error comes from assuming a linear *Ansatz* in m_π^2 for the extrapolation to the chiral limit.

From the lattice data obtained in this work R_{SM} can be estimated only in the chiral limit for the large quenched lattice. Extrapolating the results obtained in the Δ rest frame for the large quenched lattice at $Q^2=0.13$ GeV^2 we find $-\mathcal{G}_{C2}^{(a)}/\mathcal{G}_{M1}=(-7.7\pm11)\%$ which leads, via Eq. (6), to $R_{SM}=(-1.2\pm1.7)\%$ where only the statistical error is given. At $Q^2=0.126$ GeV^2 the experimental value of R_{SM} is $(-6.5\pm0.2\pm2.5)\%$ [1]. As already mentioned, the lattice evaluation of this quantity is affected by large systematic and statistical errors, which must be studied before a more accurate determination can be obtained.

Finally, in order to facilitate comparison with experiment and phenomenology, not only for the ratios but also for $\mathcal{G}_{M1}$ and $\mathcal{G}_{E2}$ separately, we give the relationship between the Sachs form factors studied in this work and the electromagnetic transition amplitudes f_{M1} and f_{E2} in the rest frame of the Δ [21]:

$$f_{M1}=\frac{e}{2m_N}\left(\frac{|\mathbf{q}|m_\Delta}{m_N}\right)^{1/2}\frac{\mathcal{G}_{M1}}{[1-q^2/(m_N+m_\Delta)^2]^{1/2}}, \qquad (34)$$

$$f_{E2}=-\frac{e}{2m_N}\left(\frac{|\mathbf{q}|m_\Delta}{m_N}\right)^{1/2}\frac{\mathcal{G}_{E2}}{[1-q^2/(m_N+m_\Delta)^2]^{1/2}} \qquad (35)$$

with $e=\sqrt{4\pi/137}$. Since these are continuum relationships to obtain results for f_{M1} and f_{E2} from the values given in Table IV one uses the physical nucleon and Δ mass. We give the values for f_{M1} and f_{E2} in Table V. They are related to the helicity amplitudes $A_{1/2}$ and $A_{3/2}$ by

$$f_{M1}=-\frac{1}{2}(A_{1/2}+\sqrt{3}A_{3/2}),$$

$$f_{E2}=-\frac{1}{2}\left(A_{1/2}-\frac{1}{\sqrt{3}}A_{3/2}\right). \qquad (36)$$

As can be seen from Table IV, the values of the helicity amplitudes for Q^2 closest to zero are in agreement with the values at $Q^2=0$, $A_{1/2}=-0.135\pm0.006$ GeV$^{-1/2}$, and $A_{3/2}=-0.255\pm0.008$ GeV$^{-1/2}$, as given by the Particle Data Group.

VI. CONCLUSIONS

The matrix element for the transition $\gamma N\rightarrow\Delta$ is computed in lattice QCD both for the quenched theory and for two

dynamical Wilson fermions in a first attempt to study unquenching effects on these form factors. The dominant magnetic dipole form factor is calculated with statistical accuracy of about 10%. The electric quadrupole is suppressed by an order of magnitude and it is calculated to a statistical accuracy of about 50%. Unquenching tends to decrease the values of $\mathcal{G}_{M1}$ and $\mathcal{G}_{E2}$. The ratio of these form factors provides a direct comparison to the experimentally measured ratio R_{EM}. We find a negative value for R_{EM} of the order of a few percent in accord with experiment. For pions of mass in the range of about 800–500 MeV we obtain no evidence for an increase in the value of R_{EM} as we unquench. It is expected that pion cloud contributions are suppressed for these heavy quarks and therefore it is important, in future studies, to use lighter dynamical quarks for the evaluation of these form factors. Large statistical and systematic errors prevent at this stage a determination of the Coulomb quadrupole form factor. A detailed study of lattice artifacts will be needed for better control of systematic errors, before a more accurate extraction of the Coulomb form factor and of the ratio R_{SM} is possible.

---

[1] C. Mertz *et al.*, Phys. Rev. Lett. **86**, 2963 (2001).

[2] K. Joo *et al.*, Phys. Rev. Lett. **88**, 122001 (2002).

[3] A. Bohr and B. Mottelson, *Nuclear Structure II* (Benjamin, Reading, MA, 1975).

[4] N. Isgur, G. Karl, and R. Koniuk, Phys. Rev. D **25**, 2394 (1982); S. Capstick and G. Karl, *ibid.* **41**, 2767 (1990).

[5] C. Alexandrou, Ph. de Forcrand, and A. Tsapalis, Phys. Rev. D **66**, 094503 (2002); Nucl. Phys. B (Proc. Suppl.) **119**, 422 (2003); Nucl. Phys. **A721**, 907 (2003); hep-lat/0309064.

[6] A.J. Buchmann and E.M. Henley, Phys. Rev. C **63**, 015202 (2001).

[7] C.N. Papanicolas, Eur. Phys. J. A **18**, 141 (2003); (private communication); A.M. Bernstein, Eur. Phys. J. A **17**, 349 (2003).

[8] G. Kälbermann and J.M. Eisenberg, Phys. Rev. D **28**, 71 (1983).

[9] C. Alexandrou *et al.*, Nucl. Phys. B (Proc. Suppl.) **119**, 413 (2003).

[10] D.B. Leinweber, T. Draper, and R.M. Woloshyn, Phys. Rev. D **48**, 2230 (1993).

[11] N. Eicker *et al.*, Phys. Rev. D **59**, 014509 (1999).

[12] H.F. Jones and M.C. Scadron, Ann. Phys. (N.Y.) **81**, 1 (1973).

[13] G.C. Gellas, T.R. Hemmert, C.N. Ktorides, and G.I. Poulis, Phys. Rev. D **60**, 054022 (1999).

[14] I. Montvay and G. Münster, *Quantum Fields on a Lattice* (Cambridge University Press, England, U.K., 1994).

[15] The factor m_Δ/E_Δ is missing in Eq. (3.25a) and in the second term of Eqs. (3.26b) and (3.27) of Ref. [10]. Equations (3.25a), (3.26b), and (3.27) as given in Ref. [10] are correct if the Δ is produced at rest.

[16] S. Güsken, Nucl. Phys. B (Proc. Suppl.) **17**, 361 (1990).

[17] C. Alexandrou, S. Güsken, F. Jegerlehner, K. Schilling, and R. Sommer, Phys. Lett. B **256**, 60 (1991).

[18] T. Draper, W. Wilcox, R.M. Woloshyn, and K.F. Liu, Nucl. Phys. **B318**, 319 (1989); Nucl. Phys. B (Proc. Suppl.) **9**, 175 (1989).

[19] Y. Iwasaki *et al.*, Phys. Rev. D **53**, 6443 (1996).

[20] T. Bhattacharya, R. Gupta, G. Kilcup, and S. Sharpe, Phys. Rev. D **53**, 6486 (1996).

[21] T. Sato and T.-S.H. Lee, Phys. Rev. C **63**, 055201 (2001); T. Sato (private communication).

[22] C. Alexandrou *et al.*, 21st International Symposium on Lattice Field Theory, Tsukuba, Ibaraki, Japan, 2003, hep-lat/0309041.

[23] C. Alexandrou, second workshop in Lattice Hadron Physics, Cairns, Australia, 2003, nucl-th/0311007.

[24] Particle Data Group, K. Hagiwara *et al.*, Phys. Rev. D **66**, 010001 (2002).

[25] D. Ardnt and B.C. Tiburzi, Phys. Rev. D **68**, 114503 (2003); **69**, 059904(E) (2004).